1

2

3

4 **Dentate Gyrus and CA3 GABAergic Interneurons Bidirectionally Modulate Signatures of**

5 **Internal and External Drive to CA1**

6

7 **Emily A. Aery Jones[1,2], Antara Rao[1,3], Misha Zilberter[1], Biljana Djukic[1], Anna K.**

8 **Gillespie[4,5], Nicole Koutsodendris[1,3], Maxine Nelson[1,2], Seo Yeon Yoon[1], Kylie Huang[1], Heidi**

9 **Yuan[1], Theodore M. Gill[1], Yadong Huang[1,2,3,6,7*], & Loren M. Frank[4,5*]**

10

11 [1]Gladstone Institute of Neurological Disease, San Francisco, CA 94158, USA.

12 [2]Biomedical Sciences Graduate Program, University of California, San Francisco, CA 94143, USA

13 [3]Developmental & Stem Cell Biology Graduate Program, University of California, San Francisco,

14 CA 94143, USA

15 [4]Kavli Institute for Fundamental Neuroscience and Department of Physiology, University of

16 California, San Francisco, CA 94143, USA

17 [5]Howard Hughes Medical Institute, Chevy Chase, MD 20815

18 [6]Departments of Neurology and Pathology, University of California, San Francisco, CA 94143,

19 USA

20 [7]Gladstone Center for Translational Advancement, San Francisco, CA 94158, USA

21

22 ***Correspondence should be addressed to:** Loren Frank (loren@phys.uscf.edu) or

23 Yadong Huang (yadong.huang@gladstone.ucsf.edu)

24 **SUMMARY**

25 Specific classes of GABAergic neurons are thought to play specific roles in regulating information

26 processing in the brain. In the hippocampus, two major classes – parvalbumin-expressing (PV$^+$)

27 and somatostatin-expressing (SST$^+$) neurons – differentially regulate endogenous firing patterns

28 and target different subcellular compartments of principal cells, but how these classes regulate the

29 flow of information throughout the hippocampus is poorly understood. We hypothesized that PV$^+$

30 and SST$^+$ interneurons in the dentate gyrus (DG) and CA3 might differentially modulate CA3

31 patterns of output, thereby altering the influence of CA3 on CA1. We found that while suppressing

32 either interneuron type increased DG and CA3 output, the effects on CA1 were very different.

33 Suppressing PV$^+$ interneurons increased local field potential signatures of coupling from CA3 to

34 CA1 and decreased signatures of coupling from entorhinal cortex to CA1; suppressing SST$^+$

35 interneurons had the opposite effect. Thus, DG and CA3 PV$^+$ and SST$^+$ interneurons

36 bidirectionally modulate the flow of information through the hippocampal circuit.

37

38 **KEYWORDS**

39 Sharp-wave ripple, hippocampus, GABAergic interneuron, parvalbumin, somatostatin, CA1,

40 CA3, dentate gyrus

41

42

43

44

45

46

47 **INTRODUCTION**

48 GABAergic interneurons regulate principal cell input and output and act as hubs for controlling

49 network activity throughout the brain (McKenzie, 2017). These interneurons are highly

50 heterogeneous (Klausberger and Somogyi, 2008), and distinct classes may play distinct roles in

51 balancing internal and external input drive to local circuits.

52 In the hippocampus, a brain structure critical for encoding, consolidation, and retrieval of

53 memories, the majority of GABAergic interneurons are either parvalbumin-expressing (PV^+) or

54 somatostatin-expressing (SST^+) (Jinno and Kosaka, 2002, 2003). PV^+ and SST^+ interneurons

55 throughout the hippocampus are distinguished by their subcellular spatial domains, firing

56 properties, pyramidal cell spike modulation mechanisms, and temporal coordination (Klausberger

57 and Somogyi, 2008). These two interneuron classes are well characterized in CA1, where they are

58 uniquely positioned to bidirectionally regulate information flow from the two major inputs:

59 internal input from CA3 and external input from entorhinal cortex (EC). PV^+ interneurons mainly

60 target somatic and perisomatic compartments and thus regulate principal cell excitability and

61 precise spike timing (Klausberger and Somogyi, 2008; Lovett-Barron et al., 2012; Miles et al.,

62 1996; Royer et al., 2012). In CA1, these cells are preferentially recruited by excitatory EC inputs

63 and are thus the main drivers of feedforward inhibition (Freund and Buzsáki, 1998; Gulyás et al.,

64 1999; Lee et al., 2016; Wheeler et al., 2015). In contrast, SST^+ interneurons mainly target distal

65 apical dendrites – which receive extrahippocampal excitatory inputs from the EC and medial

66 septum (MS) – and gate the influence of those pathways, thereby affecting the magnitude of

67 principal cell spiking (Blasco-Ibáñez and Freund, 1995; Klausberger and Somogyi, 2008; Lovett-

68 Barron et al., 2012; Sik et al., 1995, 1997; Takács et al., 2012). In CA1, these cells receive

69 primarily local inputs from pyramidal cells and thus provide feedback inhibition (Freund and

70 Buzsáki, 1998; Wheeler et al., 2015). Consistent with these patterns of inputs, potentiation of PV[+]

71 interneurons attenuates CA3 inputs while potentiation of CA1 SST[+] interneurons attenuates EC

72 inputs (Fernández-Ruiz et al., 2017; Udakis et al., 2020).

73 Whether PV[+] and SST[+] interneurons in the upstream regions of the dentate gyrus (DG) and

74 CA3 play similar distinct roles is unknown. Since both populations are inhibitory, we would expect

75 that suppressing either PV[+] or SST[+] interneurons in DG and CA3 would lead to greater total

76 spiking output from CA3 and thus greater input to CA1. Moreover, there is some overlap between

77 PV and SST expression (Jinno and Kosaka, 2000), making it unclear whether broadly manipulating

78 these genetically-defined cell classes would modulate outputs in opposing directions.

79 However, given their similarities to analogous populations in CA1 (Klausberger and

80 Somogyi, 2008), one can hypothesize that DG and CA3 PV[+] interneurons provide feed-forward

81 inhibition at the soma, thus suppressing internal DG to CA3 and CA3 to CA3 inputs. Conversely,

82 as DG and CA3 SST[+] interneurons are thought to provide feedback inhibition at the level of EC

83 inputs, we would expect them to suppress those external inputs. Thus, suppressing DG and CA3

84 PV[+] interneurons might ungate internal drive in DG and CA3, while suppressing DG and CA3

85 SST[+] interneurons might ungate external drive. If the resulting patterns of CA3 activity

86 differentially engage CA1, we would predict that suppressing either PV[+] or SST[+] interneurons in

87 DG and CA3 would enhance DG and CA3 spiking outputs, but this increase in output could have

88 different effects on CA1.

89 To measure these potential effects we took advantage of known signatures of information

90 flow in the hippocampal network. During immobility, high CA3 drive to CA1 is associated with

91 sharp-wave ripple (SWR) events (Buzsáki et al., 1992; Csicsvari et al., 2000; Ylinen et al., 1995)

92 that can be detected as increases in ripple frequency (125–200 Hz) power in CA1. Previous work

93   has shown that blocking CA3 input to CA1 reduces SWR rate, slows SWR frequency, and

94   increases multi-unit activity (MUA) recruitment to SWRs (Middleton and McHugh, 2016;

95   Nakashiba et al., 2009; Yamamoto and Tonegawa, 2017) while increasing CA3 drive to CA1

96   increases SWR rate, SWR frequency, SWR-coincident slow gamma (SG) power, and sharp wave

97   (SW) amplitude (Ramirez-Villegas et al., 2018; Wu et al., 2015). By contrast, blocking direct EC

98   input to CA1 diminishes SWR chains, but has no other observable effects on SWR rate, frequency,

99   or duration (Yamamoto and Tonegawa, 2017), while lesioning EC increases SWR rate (Bragin et

100   al., 1995a). Thus, SWR properties provide information about CA3 and EC drive to CA1, and these

101   signatures are bidirectional: decreased internal CA3 drive is associated with decreased SWR

102   activity, and decreased external EC drive is associated with increased SWR activity.

103   During movement, EC drive to CA1 is associated with fast gamma (FG; 50–100 Hz)

104   oscillations, while CA3 drive to CA1 is associated with SG (20–50 Hz) oscillations (Bragin et al.,

105   1995b; Colgin, 2016; Colgin et al., 2009). Blocking synaptic inputs from CA3 to CA1 impacts

106   CA1 SG power and modulation by theta phase while not detectably affecting CA1 SG frequency

107   and coherence across regions (Middleton and McHugh, 2016). Direct EC layer III inputs to CA1

108   have been shown to contribute to CA1 FG activity (Yamamoto et al., 2014). However, lesioning

109   inputs from CA3 to CA1 also reduces CA1 FG power, suggesting that FG may be both internally

110   and externally generated (Middleton and McHugh, 2016). SG and FG are in turn organized by

111   theta (5–11 Hz), a signature of EC and MS drive to CA1 (Colgin, 2015). Theta is not detectably

112   disrupted by blocking CA3 inputs to CA1 (Middleton and McHugh, 2016) but does diminish in

113   power and frequency throughout the hippocampus when EC is lesioned (Bragin et al., 1995b;

114   Buzsáki et al., 1983; Maurer et al., 2006; Ormond et al., 2015; Schlesiger et al., 2015). Thus, theta

115 and gamma rhythms during movement can provide information about internal CA3 and external

116 EC drive to CA1.

117 We therefore asked whether modulation of specific interneuron types in DG and CA3 could

118 alter these signatures of EC and CA3 drive to CA1. We found that while suppression of either

119 interneuron type led to an increase in DG and CA3 spiking output, suppressing PV$^+$ interneurons

120 increased signatures of CA3 coupling to CA1 and decreased those of EC coupling to CA1, while

121 suppressing SST$^+$ interneurons decreased signatures of CA3 coupling to CA1 and increased those

122 of EC coupling to CA1. Our findings indicate that PV$^+$ and SST$^+$ interneurons in DG and CA3 can

123 bidirectionally alter patterns of activity in DG and CA3, altering the balance of LFP signatures of

124 EC and CA3 drive in CA1.

125

126 **RESULTS**

127 **Recording *in vivo* hippocampal LFP during chemogenetic suppression of PV$^+$ and SST$^+$**

128 **interneurons in DG and CA3**

129 We used a Cre-dependent chemogenetic approach to silence specific interneuron classes in DG

130 and CA3. We bilaterally injected PV-Cre, SST-Cre, and PV-Cre/SST-Cre mice with AAV5-hSyn-

131 DIO-hM4D(Gi)-mCherry or with AAV5-hSyn-DIO-mCherry into the DG hilus, and then

132 implanted a 32-site silicon electrode array into the right dorsal hippocampus (Figure 1A). HM4D

133 expression was highly co-localized with PV and SST expression (Figure S1A and S1B) and

134 extended throughout DG and CA3 (Figure 1B and S1C) from dorsal to ventral hippocampus, with

135 no expression in CA1 (Figure 1C). We confirmed hM4D function in *ex vivo* brain slices by

136 observing that clozapine N-oxide (CNO) application reduced firing rates in PV$^+$ and SST$^+$

137 interneurons expressing hM4D (Figure S1D), hyperpolarized resting membrane potentials by 8.6

138   ± 1.3mV (Figure S1E), and decreased input resistance by 31.3 ± 9.9 MΩ (Figure S1F). After viral

139   expression, we recorded LFP activity from CA1, CA3, and DG over 6 daily sessions, alternating

140   CNO and vehicle treatment across days (Figure 1A). CNO was used to suppress interneuron

141   activity for the duration of the recording. We collected data from two cohorts of animals: the first

142   underwent only home cage recordings, and the second underwent linear track recordings followed

143   by home cage recordings.

144   We assessed LFP features as a readout for changes in internal CA3 versus external EC

145   drive to CA1, focusing on features previously identified to be modulated by CA3 or EC drive. We

146   took advantage of a statistical approach known as a Linear Mixed Model (LMM) to assess

147   differences between groups while accounting for variability both within and across individuals.

148   We evaluated differences between significant treatment effects to determine which effects were

149   significantly different between genotypes (referred to as specific). We further sought to control

150   our false positive rate and so only report findings which survive Holm-Bonferroni correction

151   across all comparisons in each experiment (see Methods).

152

153   **Suppressing PV$^+$ or SST$^+$ interneurons bidirectionally modulates SWR signatures of CA3**

154   **coupling to CA1**

155   We first asked whether PV$^+$ or SST$^+$ interneurons in DG and CA3 modulate signatures of CA3

156   coupling to CA1 as measured through increased SWR activity during immobility (<1 cm/s for ≥30

157   s) in 1-hour daily home cage sessions (Figure 2A). We hypothesized that suppressing DG and CA3

158   PV$^+$ interneurons might ungate internal DG and CA3 inputs and thus changing DG and CA3 firing

159   patterns in a manner that facilitates internally driven patterns of activity (e.g. SWRs) in CA1.

160   Conversely, suppressing DG and CA3 SST[+] interneurons might ungate EC inputs and perhaps

161   change DG and CA3 firing patterns in a manner that increases CA1 receptivity to EC drive.

162   We began by measuring the effect of interneuron suppression on SWR recruitment and

163   found that suppressing either class increased DG and CA3, but not CA1, MUA activity during

164   SWRs (Figure 2B). Thus, suppressing these interneurons unidirectionally disinhibited local DG

165   and CA3 cells while leaving CA1 spiking intact. As SWRs depend on CA3 input to CA1, one

166   might predict that SWR events themselves would be more prevalent following suppression of

167   either PV[+] or SST[+] interneurons.

168   This was not the case. Instead, we found evidence for opposing modulation of SWRs by

169   PV[+] and SST[+] interneurons in DG and CA3. Suppressing PV[+] interneurons increased SWR rate

170   while suppressing SST[+] interneurons decreased SWR rate, and these effects were significantly

171   different between genotypes (Figure 2C). This effect was not due to differences in SWR detection

172   or baseline MUA (Table S1). There was also a decrease in the proportion of SWRs that participated

173   in chains (Figure 2D) in both genotypes, indicating that broadly increasing DG and CA3 output

174   influences chaining of SWRs. Finally, we examined fast ripples (Valero et al., 2017) to determine

175   whether the observed changes in SWR rate were due to epileptic activity, as ablation or silencing

176   of CA1 or subiculum interneurons can lead to seizures (Drexel et al., 2017; Spampanato and

177   Dudek, 2017). While we observed no behavioral seizures, we did detect a modest increase in the

178   incidence of rare fast ripples when PV[+] interneurons were suppressed (Table S1), indicating that

179   increased CA3 drive might increase potentially pathological SWRs.

180   We then assessed the structure of these SWRs and found further evidence for interneuron

181   subtype-specific effects. SST[+] interneuron suppression increased SWR length, an effect not seen

182   following PV+ interneuron suppression (Figure 2E). Since EC activity can increase prior to SWRs

183   longer than 100 ms (Oliva et al., 2018), we also looked specifically at the proportion of SWRs

184   longer than 100 ms and found an increase when SST[+] interneurons were suppressed (% of SWRs

185   > 100 ms: vehicle 38.5% vs CNO 49.6%, paired t test, $t(15) = 3.67$, $p = 0.002$). Thus, suppressing

186   DG and CA3 SST[+] interneurons has effects consistent with facilitated EC input to CA1.

187   Similar differences were seen for other SWR parameters. PV[+] interneuron suppression

188   alone increased instantaneous frequency of SWRs in CA1 (Figure 2F), but decreased the

189   instantaneous frequency of SWRs in CA3 (Figure S2A), thus the local and downstream effects of

190   these interneurons can be different. During SWRs, PV[+] interneuron suppression increased sharp-

191   wave (SW) amplitude in CA1, which was specific for this cell type (Figure 2G). However, SWR

192   size was smaller when PV[+] interneurons were suppressed (Figure S2B) despite no change in CA1

193   MUA recruitment. Overall, suppressing PV[+] interneurons increased SWR signatures of CA3 drive

194   to CA1, while suppressing SST[+] interneurons decreased these signatures, consistent with a role in

195   external drive to DG and CA3 and thereby facilitating external drive to CA1.

196

197   **Suppressing PV[+] or SST[+] interneurons bidirectionally modulates SWR-coincident SG**

198   **signatures of CA3 coupling to CA1**

199   Next, we measured SG power coincident with ripples, which is driven by CA3 (Carr et al., 2012;

200   Gillespie et al., 2016; Ramirez-Villegas et al., 2015, 2018). Based on the results above, we again

201   hypothesized that suppressing PV[+] interneurons would have similar effects to increasing CA3

202   drive to CA1, while suppressing SST[+] interneurons would have similar effects to increasing EC

203   drive to CA1.

204   Following suppression of PV[+] interneurons, SG power in CA1 was higher across all rest

205   during CNO epochs (Figure 3A) – a signature of increased CA3 drive (Kemere et al., 2013) – and

206   had higher variance in all 3 subregions (Table S2). We therefore used the mean and SD of SG

207   power calculated from vehicle-treated epochs to z-score SG power during all epochs. Suppressing

208   PV^+ interneurons led to greater SWR-coincident SG power in CA1, CA3, and DG (Figure 3A, 3B,

209   3D, and S2C). Interestingly, the extent of CA1 SWR-coincident SG power increase correlated

210   across animals with the extent of SW amplitude increase and the extent of SWR frequency increase

211   (Figure S2D–E), suggesting these features reflect similar underlying mechanisms, as has been

212   suggested previously (Oliva et al., 2018; Stark et al., 2014). These effects were specific to PV^+

213   interneurons, as suppressing SST^+ interneurons did not change SG power either at baseline (Table

214   S1) or during SWRs (Figure 3A, 3C, 3D, and S2C). Similarly, only PV^+ suppression enhanced the

215   increase in SG coherence between CA1 and CA3 or DG during SWRs, (Figure 3E); this was not

216   merely due to increases in activity as CA1 MUA did not increase (Figure 2B). Overall, suppressing

217   PV^+ interneurons increased SWR activity, consistent with a facilitation of internally generated

218   CA3 spiking patterns that lead to SWRs, while suppressing SST^+ interneurons decreased SWR

219   activity, consistent with a role in ungating EC inputs to DG and CA3 and thereby changing DG

220   and CA3 firing patterns in a manner that suppressed SWR activity.

221

222   **Suppressing PV^+ or SST^+ interneurons bidirectionally modulates SG signatures of CA3**

223   **coupling to CA1 during movement**

224   We next asked whether these bidirectional effects extended to LFP features observed during

225   movement. We examined CA1 SG, FG, and theta activity during movement (>1 cm/s) in daily 30-

226   minute linear track sessions, focusing on stratum pyramidale (Figure 4A), though similar results

227   were found in recordings from strata radiatum (where CA3 inputs terminate) and lacunosum

228   moleculare (where EC inputs terminate; data not shown). We asked whether suppressing DG and

229   CA3 PV$^+$ interneurons ungates internally driven CA3 activity patterns, while suppressing DG and

230   CA3 SST$^+$ interneurons ungates EC inputs and thus change firing patterns in a manner that

231   facilitates increasing EC drive to CA1.

232   We again began by measuring the effect of interneuron suppression on spiking output and

233   found that suppressing either class increased MUA during movement in DG and CA3, but not CA1

234   (Figure 4B). Thus, just as for SWR-related activity, suppressing interneurons unidirectionally

235   disinhibited local DG and CA3 cells while leaving CA1 spiking rates intact.

236   Despite this, we found that PV$^+$ and SST$^+$ interneurons differentially modulated SG during

237   movement. Suppressing PV$^+$ interneurons in DG and CA3 amplified SG power in CA1, but there

238   was no detectable effect following suppression of SST$^+$ interneurons. By contrast, suppressing PV$^+$

239   interneurons had no detectable effect on SG power in DG and CA3, while suppressing SST$^+$

240   interneurons dampened SG power locally in DG and CA3. All these effects were significantly

241   different across genotypes (Figure 4B–C and S3A). Relatedly, suppressing PV$^+$ interneurons

242   enhanced SG coherence between CA1 and CA3 (Figure 4D). Thus, like during rest periods,

243   suppressing PV$^+$ interneurons increased the amplitude of SG in CA1 and the coherence of SG,

244   across regions, consistent with an increase of CA3 drive to CA1. In addition, suppressing PV$^+$

245   interneurons, but not SST$^+$ interneurons, reduced SG frequency throughout the hippocampus

246   (Figure 4E and S3B). Finally, suppressing PV$^+$ interneurons increased theta modulation of SG only

247   locally in DG and CA3, while suppressing SST$^+$ interneurons reduced theta modulation of SG in

248   CA1, and these effects were again detectably different between genotypes. Overall, suppressing

249   PV$^+$ interneurons amplified SG while suppressing SST$^+$ interneurons had the opposite effect.

250

Suppressing PV$^+$ or SST$^+$ interneurons bidirectionally modulates FG signatures of EC coupling to CA1 during movement

The results above indicate that suppressing PV$^+$ or SST$^+$ interneurons in DG and CA3 can lead to quite different effects in CA1, despite the increase in DG and CA3 multiunit activity seen in both cases. As described above, a potential for these differences is that these two interneuron classes differentially effect the organization of activity transmitted from CA3 to CA1, and thereby have different effects on CA1. If so, then suppressing SST$^+$ interneurons in DG and CA3 would also enhance FG in CA1, despite this typically being characterized as a signature of direct EC input to CA1 (Colgin, 2016). Further, if this hypothesis is correct, then suppressing PV$^+$ interneurons in DG and CA3 would have the opposite or no effect, as this would facilitate internally, rather than externally, driven patterns in DG and CA3.

Our data provided strong support for that possibility. Suppressing SST$^+$ interneurons amplified FG power in CA1 and DG, an effect specific to this interneuron class (Figure 5A–B and S3D). Interestingly, locally in DG and CA3, suppression of SG in SST-Cre mice appeared to mirror enhancement of FG, where animals with the greatest SG suppression showed the greatest FG enhancement and vice versa (Figure S3E). This suggests that these two signatures of input drive may be opposing, with modulations that decrease SG power leading to greater FG power. Overall, these bidirectional changes in SG and FG power led to decreased SG/FG power ratios in CA1 following SST$^+$ suppression and increased SG/FG power ratios throughout the hippocampus following PV$^+$ suppression. These SG/FG ratio effects were significantly different between genotypes across the hippocampus (Figure 5C–E and S3F). FG coherence, however, did not change (Figure 5F). In addition, suppressing SST$^+$ interneurons increased FG frequency throughout the hippocampus (Figure 5G and S3G). Finally, suppressing SST$^+$ interneurons

274   increased theta modulation of FG in CA1 (Figure 5H–J and S3H), an effect which was specific to

275   SST$^+$ interneurons. Overall, suppressing SST$^+$ interneurons increased CA1 FG activity – a

276   signature of EC drive – while suppressing PV$^+$ interneurons had opposing effects. These effects

277   suggest a role for the CA3 input as a modulator of FG in CA1.

278

279   **Suppressing PV$^+$ or SST$^+$ interneurons unidirectionally modulates theta during movement**

280   Next, we asked whether PV$^+$ and SST $^+$ interneurons might regulate theta. Previous work has

281   suggested that theta throughout the hippocampus is driven by EC and MS inputs, but not by CA3

282   inputs (Colgin, 2016; Middleton and McHugh, 2016). Consequently, we predicted that suppressing

283   SST$^+$ interneurons would enhance theta power in DG and CA3 only, perhaps through ungating EC

284   inputs, while suppressing PV$^+$ interneurons would have no effect. Contrary to our hypothesis,

285   suppressing either PV$^+$ or SST$^+$ interneurons increased theta power in CA1 but not elsewhere

286   (Figure S4A–B). Neither interneuron type modified theta coherence (Figure S4C) or theta

287   frequency (Figure S4D) save for an increase in theta frequency in PV-Cre mice in DG. These

288   findings suggest that a general increase in CA3 spiking output increases CA1 theta power.

289   Overall, suppressing PV$^+$ interneurons in DG and CA3 increased measures of CA3

290   coupling onto CA1, including enhancing SG power, coherence, and theta comodulation and

291   dampening FG-theta comodulation. In contrast, suppressing SST$^+$ interneurons in DG and CA3

292   increased measures of EC coupling onto CA1, including enhancing FG power and theta coupling

293   and dampening SG power and theta coupling. Suppressing either interneuron type enhanced CA1

294   theta power.

295

296   **Suppressing both PV$^+$ and SST$^+$ interneurons increases CA3 coupling onto CA1**

297   Lastly, we assessed the effect of suppressing both interneuron populations simultaneously in PV-

298   Cre/SST-Cre mice (Figure S5 and S6 and Table S4). Ablating AMPA currents to all hippocampal

299   interneurons increases SWR rate and frequency (Caputi et al., 2012), similar to DG and CA3 PV$^+$

300   interneuron suppression (Figure 2C and 2F). Thus, we hypothesized that suppressing both

301   interneuron types would follow suppressing only PV$^+$ interneurons. In all measures except for

302   comodulation of SG by theta in DG and CA3, we were unable to detect a difference between

303   suppressing both interneuron types and suppressing PV+ interneurons only. In this instance,

304   suppressing both interneuron types decreased theta modulation of SG, an effect not observed when

305   suppressing either type alone. In contrast, we were able to detect several differences between

306   suppressing both interneuron types and suppressing SST+ interneurons only. FG frequency and

307   CA1 FG power are notable exceptions, in which case suppressing both interneuron types followed

308   the direction of suppressing SST+ interneurons alone.

309

310   **Consistency of effect across genotypes and sexes**

311   To assess the robustness of these effects, we first assessed both males and females, since females

312   have more DG interneurons than males at this age (Leung et al., 2012). Females had slightly higher

313   SWR sizes than males during vehicle treatment epochs (Table S5), but there were otherwise no

314   sex differences. The effect of suppressing interneurons was in the same direction and magnitude

315   in both sexes on most features (Table S6) with a few exceptions. Suppressing SST$^+$ interneurons

316   decreased SW amplitude in females but had the opposite effect in males, leading to no effect

317   overall, and enhanced FG power to a greater degree in females than in males. Interestingly,

318   suppressing either or both interneuron classes led to a greater increase in DG and CA3 MUA during

319   movement in females; though it did not have functional consequences, this underlines the need for

320   sex-specific analyses in manipulation experiments. With those minor exceptions, the observed

321   effects do not appear to be driven mainly in animals of a particular sex.

322   We further verified that differences in LFP during movement were not due to differences

323   in running speed (vehicle 4.8 cm/s vs CNO 5.1 cm/s, paired t test, t(29) = 1.31, p = 0.2). Then, we

324   confirmed that none of these effects could be confounded by differences between genotypes during

325   vehicle treatment sessions (Table S3). We did note, however, that PV-Cre had different DG and

326   CA3 SG frequencies and SG/FG ratios from SST-Cre mice during vehicle treatment (Table S3),

327   but since the direction of this difference was opposite from the direction of treatment effect, it does

328   not affect our interpretation. Finally, to control for possible off-target effects of CNO, we treated

329   mice injected with an empty vector as a control and observed no differences between vehicle and

330   CNO treated epochs (Figure S5 and S6 and Table S4).

331

DISCUSSION

333   We carried out targeted inhibition of PV$^+$ or SST$^+$ interneurons in the DG and CA3 regions of the

334   hippocampus and found clear evidence for differential effects on activity in downstream CA1. Our

335   findings provide evidence that PV$^+$ and SST$^+$ interneurons in DG and CA3 differentially regulate

336   information flow through the hippocampus: suppression of PV$^+$ interneurons increased signatures

337   of internal drive associated with CA3 input to CA1 while suppression of SST$^+$ interneurons

338   increased signatures of external drive associated with EC input to CA1 (Figure 6). These

339   bidirectional effects were observed despite both interneuron classes increasing the spiking output

340   of DG and CA3 without changing spiking rates in CA1.

341   Specifically, suppressing PV$^+$ interneurons led to SWR and SG/FG modulation consistent

342   with increasing CA3 drive and decreasing EC drive to CA1: SWRs seen during immobility had

343 higher incidence, faster frequency, greater amplitude of coincident SWs and SG, and showed

344 higher SG coherence across regions; SG during movement had greater power and coherence

345 across regions while FG during movement had reduced modulation by theta. These findings concur

346 with two recent studies which modulated CA3 PV$^+$ interneurons in rats and *ex vivo* (Antonoudiou

347 et al., 2020; López-Madrona et al., 2020). By contrast, suppressing SST$^+$ interneurons led to SWR

348 and SG modulation consistent with decreasing CA3 drive and increasing EC drive to CA1: SWRs

349 had lower incidence and greater length, while SG during movement had reduced modulation by

350 theta and FG during movement had greater power. Changes in LFP signatures in DG and CA3

351 were largely consistent with CA1, suggesting these patterns of activity changed locally and then

352 propagated.

353 These roles are remarkably similar to those identified for PV$^+$ and SST$^+$ interneurons in

354 CA1, where PV$^+$ interneurons regulate CA3 drive and SST$^+$ interneurons regulate EC drive

355 (Fernández-Ruiz et al., 2017; Udakis et al., 2020). We therefore hypothesize that across the

356 hippocampus, PV$^+$ and SST$^+$ interneurons are likely to be modulated coherently as different flows

357 of information are needed. Importantly, clear differences were observed following inhibition of

358 the two interneuron subtypes despite the existence of substantial variation within interneuron

359 classes (Harris et al., 2018; Klausberger and Somogyi, 2008) and the presence of PV and SST co-

360 expressing cells (Jinno and Kosaka, 2000), suggesting overarching roles for PV$^+$ and SST$^+$

361 interneurons in DG and CA3 in regulating information flow through the hippocampal network.

362 Our findings also identify a dissociation between overall activity levels in CA3 and

363 signatures of CA3 drive in CA1. Suppressing SST$^+$ interneurons, which we hypothesized would

364 ungate EC inputs to DG and CA3, led to an increase CA3 multiunit activity. Despite that increase,

365 we observed a decrease in signatures of CA3 input to CA1 but an increase in FG, a signature of

366   direct EC input to CA1 (Colgin, 2016). Importantly, this dissociation between activity and

367   influence is are consistent with the observation of reduced FG signatures of EC drive to CA1

368   following CA3 silencing (Middleton and McHugh, 2016). These findings suggest that FG in CA1,

369   rather than a pure signature of EC drive to CA1, is best understood as a signature of overall EC

370   drive to both CA1 and the upstream DG and CA3 network. More broadly, these findings highlight

371   the likely importance of specific patterns of CA3 spiking in influencing CA1: suppression of both

372   interneuron types lead to increases in CA3 output but opposite effects on CA3- versus EC-

373   associated LFP patterns in CA1. This is most likely a result of the engagement of different patterns

374   of CA3 spiking.

375   In controlling input drive, these interneuron classes may regulate hippocampal information

376   processing. The hippocampus contributes to encoding, consolidation, and retrieval of memories,

377   and is thought to alternate between three distinct network states in order to do so (Buzsáki, 1989;

378   Kay and Frank, 2019; Sosa et al., 2018). Encoding of new information is driven by external inputs

379   from the EC, consolidation of previous information by internal inputs from the CA3, and retrieval

380   by a combination of EC and CA3 inputs (Carr and Frank, 2012). Thus, inteneuron-mediated

381   alterations in the strengths of these two inputs could help support different memory functions.

382   Consistent with this possibility, previous behavioral studies examining DG and CA3 PV^+ and SST^+

383   interneurons during contextual threat conditioning support the hypothesis that PV^+ interneuron

384   suppression could support consolidation by ungating internal CA3 input while SST^+ interneuron

385   suppression could support encoding by ungating external EC input (Guo et al., 2018; Stefanelli et

386   al., 2016; Zou et al., 2016). In sum, the hippocampal circuit may engage or disengage PV^+ and

387   SST^+ interneurons during appropriate learning phases to alter the balance between CA3 and EC

388   inputs and thereby support consolidation or encoding processes.

389   Previous studies of the CA1 LFP signatures further illustrate how DG and CA3 PV[+] and

390   SST[+] interneurons might modulate learning and memory processes. First, suppressing SST[+]

391   interneurons reduced SWR rate, which might reduce learning, as abolishing SWRs disrupts

392   learning (Ego-Stengel and Wilson, 2010; Girardeau et al., 2009; Jadhav et al., 2012) and lower

393   SWR rate predicts memory impairments in Alzheimer's models(Jones et al., 2019). However, we

394   found that suppressing SST[+] interneurons also lengthened SWRs, which may increase the length

395   of the underlying replay trajectory and improve working memory (Fernández-Ruiz et al., 2019).

396   In contrast, suppressing PV[+] interneurons increased fast ripple incidence, which may be a

397   pathological conversion from SWRs (Behrens et al., 2007; Foffani et al., 2007) which in turn could

398   disrupt normal encoding (Ewell et al., 2019). However, suppressing PV[+] interneurons heightened

399   the extent to which SG coherence increased during SWRs, which is associated with greater replay

400   fidelity (Carr et al., 2012). Finally, suppressing PV[+] interneurons increased SG power, which could

401   support retrieval following task learning (Muzzio et al., 2009; Tort et al., 2009), while suppressing

402   SST[+] interneurons increased FG power and modulation by theta, which could support encoding of

403   new locations (Zheng et al., 2016) and working memory maintenance (Axmacher et al., 2010).

404   Future experiments should examine if there is a casual relationship between activity of these

405   GABAergic populations and spatial task performance.

406   SST[+] interneurons in the DG are specifically lost in Alzheimer's disease and normal aging

407   models, and the extent of their loss correlates with memory impairments (Andrews-Zwilling et al.,

408   2010; Leung et al., 2012; Spiegel et al., 2013). These models show reduced SWR rate, frequency,

409   and coincident SG power (Cayzac et al., 2015; Ciupek et al., 2015; Cowen et al., 2018; Gillespie

410   et al., 2016; Iaccarino et al., 2016; Nicole et al., 2016; Wiegand et al., 2016), and the extent of

411   these impairments predicts memory deficits (Jones et al., 2019). Suppression of DG and CA3 SST[+]

412   interneurons induces similar changes in SWR characteristics, serving as further evidence that loss

413   of these interneurons may be directly responsible for SWR alterations in pathological and normal

414   aging and related memory deficits.

415   Beyond the hippocampus, many other brain regions facilitate multiple information

416   processing roles through a balance of inputs. This could also be modulated by PV^+ and SST^+

417   interneurons, as they have been shown to have distinct and often bidirectional roles in cortex.

418   Specifically, this is found in tuning (Miao et al., 2017; Wilson et al., 2012), beta and theta

419   frequency activity (Chen et al., 2017), stimulus-induced gamma rhythms (Hakim et al., 2018; Veit

420   et al., 2017), slow waves and spindles (Funk et al., 2017; Kuki et al., 2015; Niethard et al., 2018),

421   NREM (Funk et al., 2017), reward encoding (Kvitsiani et al., 2013), and working memory (Abbas

422   et al., 2018; Kim et al., 2016). These results are broadly consistent with our results showing

423   bidirectional modulation of signatures of internal and external inputs by DG and CA3 PV^+ and

424   SST^+ interneuron populations, and we suggest that the distinction between internal and external

425   drive may be useful in understanding the roles of these interneurons outside the hippocampus.

426

435

AUTHOR CONTRIBUTIONS

E.A.A.J., Y.H., and L.M.F. designed and coordinated the study. E.A.A.J. carried out most studies, performed all data analysis, and created all figures. E.A.A.J. and L.M.F wrote the manuscript. A.K.G. and A.R. assisted with *in vivo* electrophysiological recordings. M.Z. and B.D. performed *ex vivo* electrophysiology experiments. A.R., N.K., M.N., and H.Y. assisted with immunohistochemistry. S.Y.Y. managed mouse lines and performed perfusions. K.H. and T.M.G. assisted with behavioral task design and provided advice on data analysis. Y.H. and L.M.F. provided advice on data analysis and interpretations, edited the manuscript, and supervised the project.

DECLARATION OF INTERESTS

Y.H. is a co-founder and scientific advisory board member of E-Scape Bio, Inc., GABAeron, Inc., and Mederon Bio, LLC. Other authors declare no competing financial interests.

Figure 1
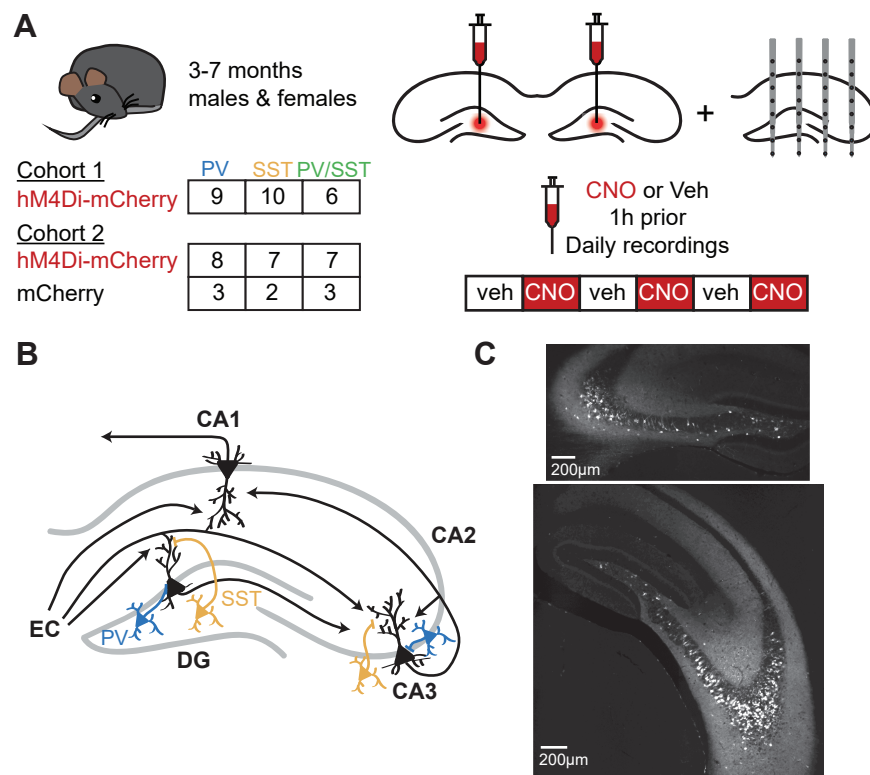
458   **FIGURE LEGENDS**

459   **Figure 1. Recording *in vivo* hippocampal LFP during chemogenetic suppression of PV[+] and**

460   **SST[+] interneurons in DG and CA3.**

461   (A) Experimental strategy. Mice were bilaterally injected with AAV5-hSyn-DIO-hM4D(Gi)-

462   mCherry or with AAV5-hSyn-DIO-mCherry into the DG hilus, then implanted with a 32-site

463   silicon electrode array into the right dorsal hippocampus. LFP activity was recorded from all

464   hippocampal subregions over 6 daily 1 hour sessions, alternating CNO and vehicle treatment.

465   (B) Simplified circuit diagram of the hippocampus. DG and CA3 receive excitatory inputs from

466   EC layer II onto distal dendrites and inhibitory inputs from local PV[+] interneurons (blue) onto the

467   soma and local SST[+] interneurons (yellow) onto distal dendrites. CA1 receives direct input from

468   EC layer III, indirect input from EC layer II via DG and CA3, and input from CA3. Adapted with

469   permission from (Gillespie et al., 2016).

470   (C) Example of mCherry expression in dorsal (top) and ventral (bottom) hippocampus.

471   See also Figure S1.

472

473

474

475

476

477

478

479
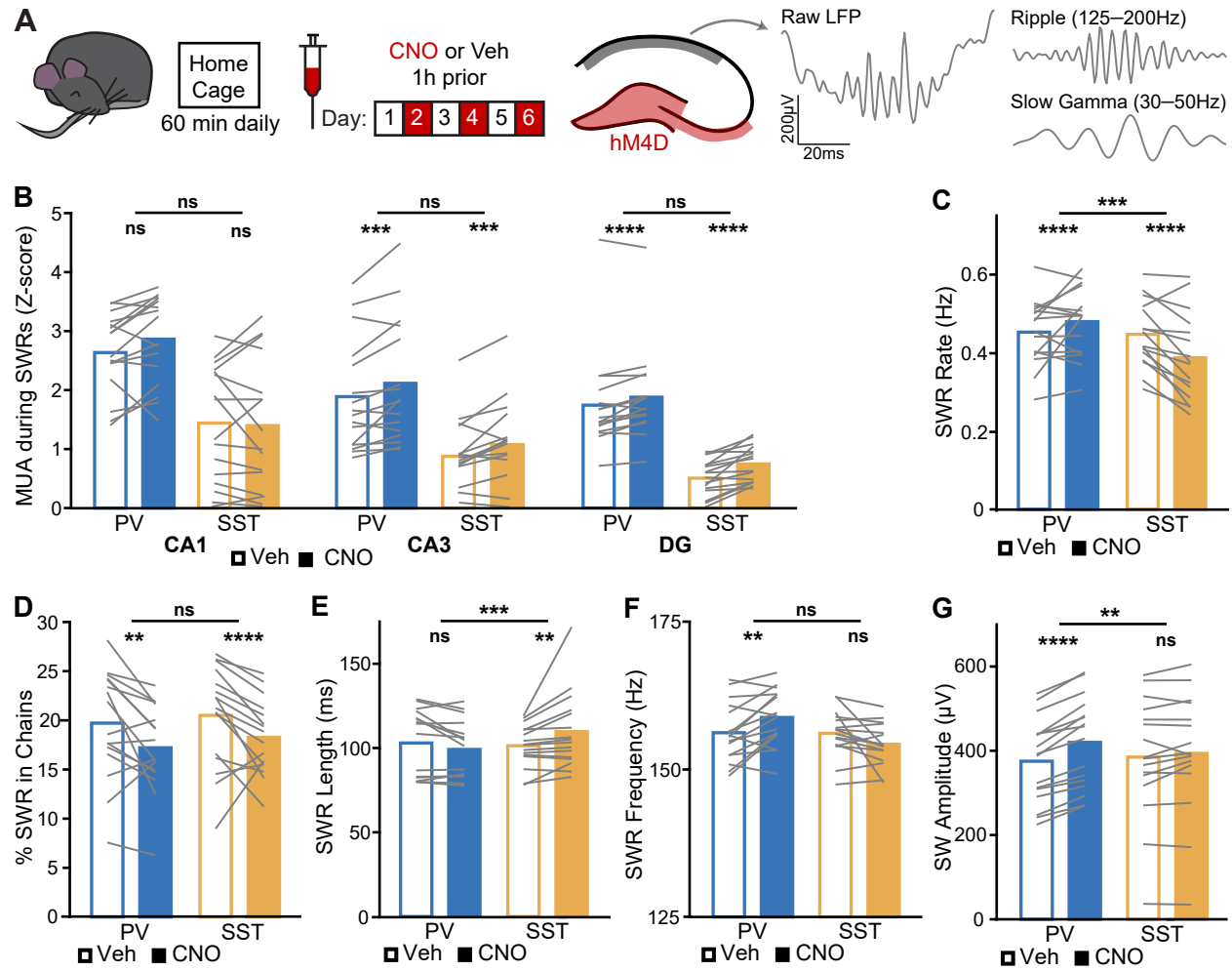
Figure 2

480   **Figure 2. Suppressing PV$^+$ or SST$^+$ interneurons bidirectionally modulates SWR signatures**

481   **of CA3 coupling to CA1.**

482   (A) Mice were recorded during sleep and awake rest over 6 daily home cage sessions, alternating

483   vehicle and CNO treatment. Interneurons in DG and CA3 (cyan) were inhibited while SWRs and

484   related oscillations were assessed in CA1 stratume pyramidale (pyr) and stratum radiatum (sr)

485   (magenta). Representative raw, ripple filtered, and SG filtered traces of a SWR event from a CA1-

486   pyr site of a PV-Cre/SST-Cre mouse during vehicle treatment.

487   (B) Normalized recruitment to SWRs of MUA in CA1 (PV: p = 0.13; SST: p = 0.46; PV vs SST:

488   p = 0.023), CA3 (PV: p = 0.00075; SST: p = 0.00076; PV vs SST: p = 0.095), and DG (PV: p =

489   5.5×10^{-6}; SST: p = 3.4×10^{-5}; PV vs SST: p = 0.059).

490   (C) SWR rate (PV: p = 1.9×10^{-6}; SST: p = 4.6×10^{-5}; PV vs SST: p = 0.00098).

491   (D) Percent of SWRs following another SWR within 200 ms (PV: p = 0.001; SST: p = 2.5×10^{-5};

492   PV vs SST: p = 0.99).

493   (E) SWR temporal length (PV: p = 0.033; SST: p = 0.0023; PV vs SST: p = 0.00034).

494   (F) SWR instantaneous frequency (PV: p = 0.0012; SST: p = 0.033; PV vs SST: p = 0.018).

495   (G) SW amplitude (PV: p = 6.4×10^{-27}; SST: p = 0.25; PV vs SST: p = 0.005).

496   N = 16 PV-Cre and n = 16 SST-Cre mice. Statistical details in Table S2. F test of the LMM for

497   treatment effects, likelihood ratio test for genotype-treatment interaction effects. **p < 0.01; ***p

498   < 0.001; ****p < 0.0001. Central values are means and individual points are mean per animal. See

499   also Figures S2 and 6 and Tables S1–S6.

500

501
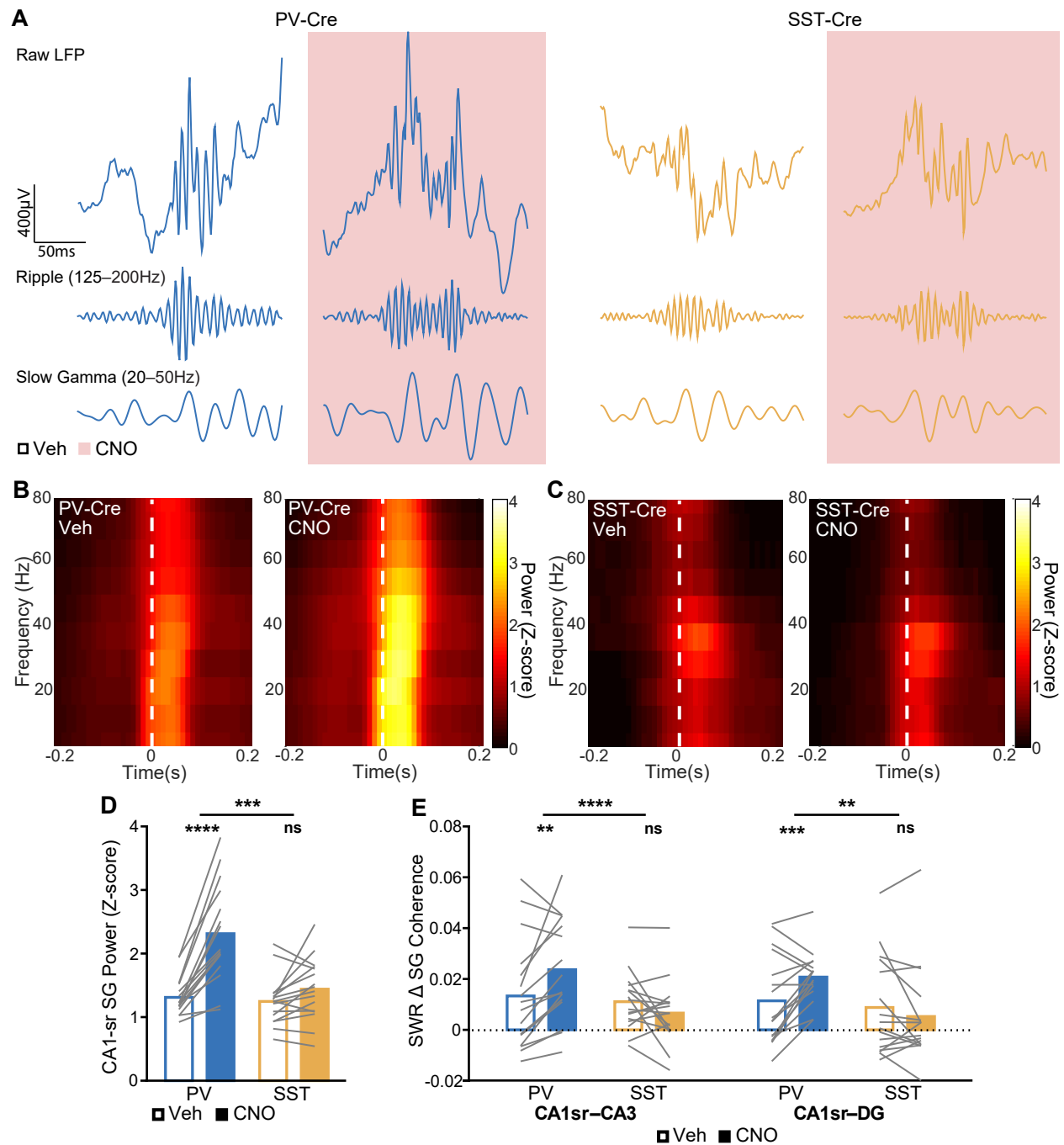
Figure 3

502 **Figure 3. Suppressing PV⁺ or SST⁺ interneurons bidirectionally modulates SWR-coincident**

503 **SG signatures of CA3 coupling to CA1.**

504 (A) Example raw (top), SWR-filtered (middle), and SG-filtered (bottom) LFP traces from CA1

505 pyramidal layer sites from a PV-Cre (left) and an SST-Cre (right) mouse. SG power is higher both

506 outside of and during SWRs in PV-Cre mice following CNO treatment.

507 (B,C) Representative SWR-triggered spectrograms from a CA1-sr layer site during vehicle-treated

508 epochs (left) and CNO-treated epochs (right) in (A) a PV-Cre mouse and (B) an SST-Cre mouse.

509 White dash lines represent threshold crossing for SWR detection.

510 (D) Normalized SG power during SWRs in CA1 (PV: $p = 1.7 \times 10^{-23}$; SST: $p = 0.14$; PV vs SST: p

511 $= 0.00099$).

512 (E) Increase during SWRs of SG frequency band coherence between CA1 and CA3 (PV: $p =$

513 0.0011; SST: $p = 0.17$; PV vs SST: $p = 9.4 \times 10^{-6}$) and between CA1 and DG (PV: $p = 0.00097$;

514 SST: $p = 0.43$; PV vs SST: $p = 0.0036$).

515 N = 16 PV-Cre and n = 16 SST-Cre mice. Statistical details in Table S2. F test of the LMM for

516 treatment effects, likelihood ratio test for genotype-treatment interaction effects. $**p < 0.01$; $***$p

517 < 0.001; $****p < 0.0001$. Central values are means and individual points are mean per animal. See

518 also Figures S2 and 6 and Tables S1–S6.

519

520

521

522

523
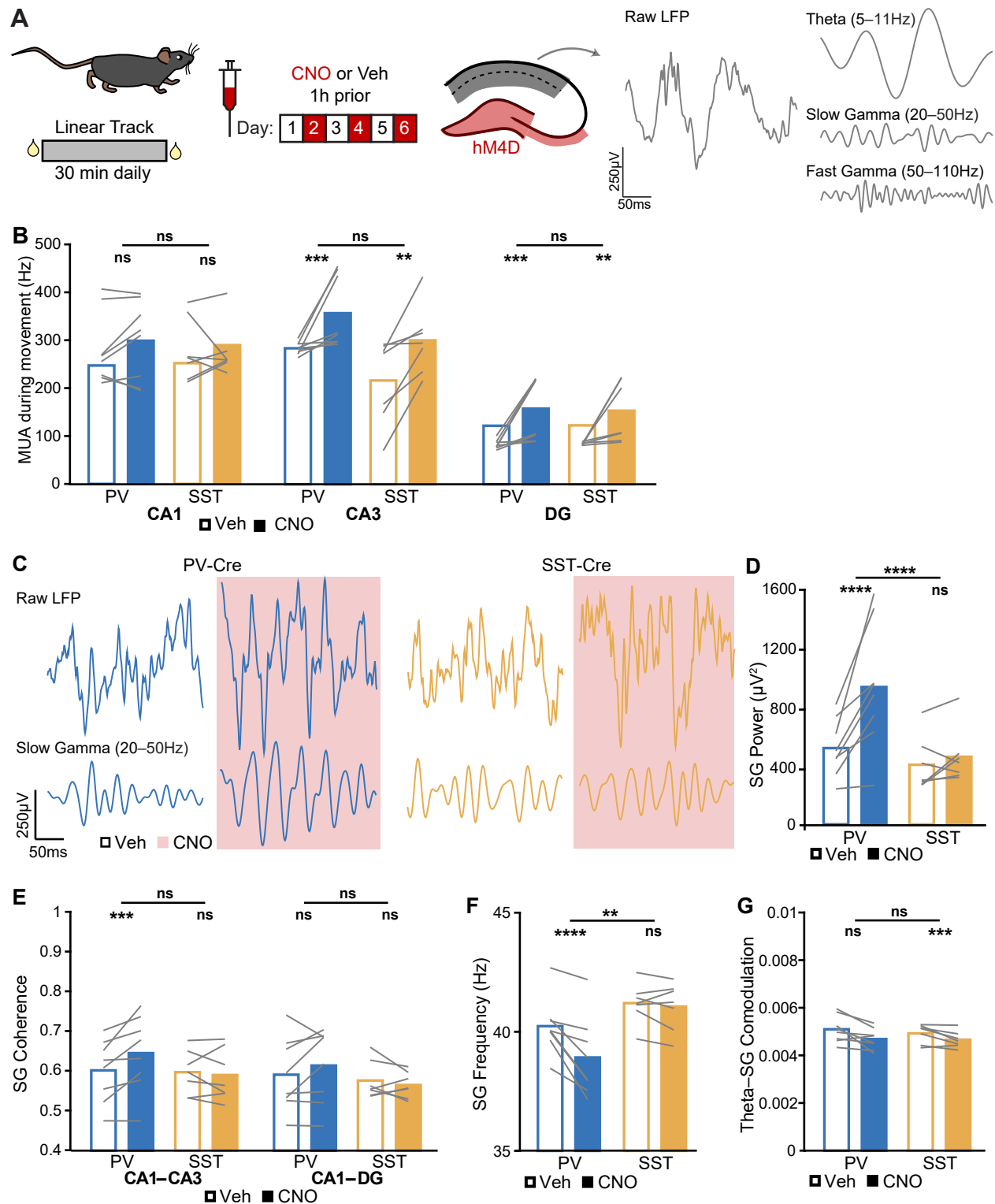
Figure 4

524 **Figure 4. Suppressing PV$^+$ or SST$^+$ interneurons bidirectionally modulates SG signatures of**

525 **CA3 coupling to CA1 during movement**.

526 (A) Mice were recorded during linear track runs over 6 daily sessions, alternating vehicle and CNO

527 treatment. Interneurons in DG and CA3 (cyan) were inhibited while theta and gamma oscillations

528 were assessed in CA1-pyr, CA1-sr, and CA1 stratum lacunosum-moleculare (slm) (magenta).

529 Representative raw trace and LFP filtered for theta, SG, and FG from a CA1-pyr site of a PV-Cre

530 mouse during movement during vehicle treatment.

531 (B) MUA during movement in CA1 (PV: $p = 0.72$; SST: $p = 0.9$; PV vs SST: $p = 0.34$), CA3 (PV:

532 $p = 0.00051$; SST: $p = 0.005$; PV vs SST: $p = 0.87$), and DG (PV: $p = 0.00022$; SST: $p = 0.0063$;

533 PV vs SST: $p = 0.59$).

534 (C) Example raw (top) and SG-filtered (bottom) LFP traces from CA1 pyramidal layer sites from

535 a PV-Cre (left) and an SST-Cre (right) mouse.

536 (D) SG power (PV: $p = 2.6 \times 10^{-6}$; SST: $p = 0.13$; PV vs SST: $p = 4.7 \times 10^{-6}$).

537 (E) SG frequency band coherence between CA1 and CA3 (PV: $p = 0.00028$; SST: $p = 0.6$; PV vs

538 SST: $p = 0.56$) and between CA1 and DG (PV: $p = 0.085$; SST: $p = 0.3$; PV vs SST: $p = 0.26$).

539 (F) SG instantaneous frequency (PV: $p = 2.5 \times 10^{-6}$; SST: $p = 0.56$; PV vs SST: $p = 0.0061$).

540 (G) Theta modulation of SG power (PV: $p = 0.12$; SST: $p = 0.00082$; PV vs SST: $p = 0.95$).

541 N = 8 PV-Cre and n = 7 SST-Cre mice. Statistical details in Table S2. F test of the LMM for

542 treatment effects, likelihood ratio test for genotype-treatment interaction effects. **$p < 0.01$; ***p

543 < 0.001; ****$p < 0.0001$. Central values are means and individual points are mean per animal. See

544 also Figures S3, S4, and 6 and Tables S2–S6.

545
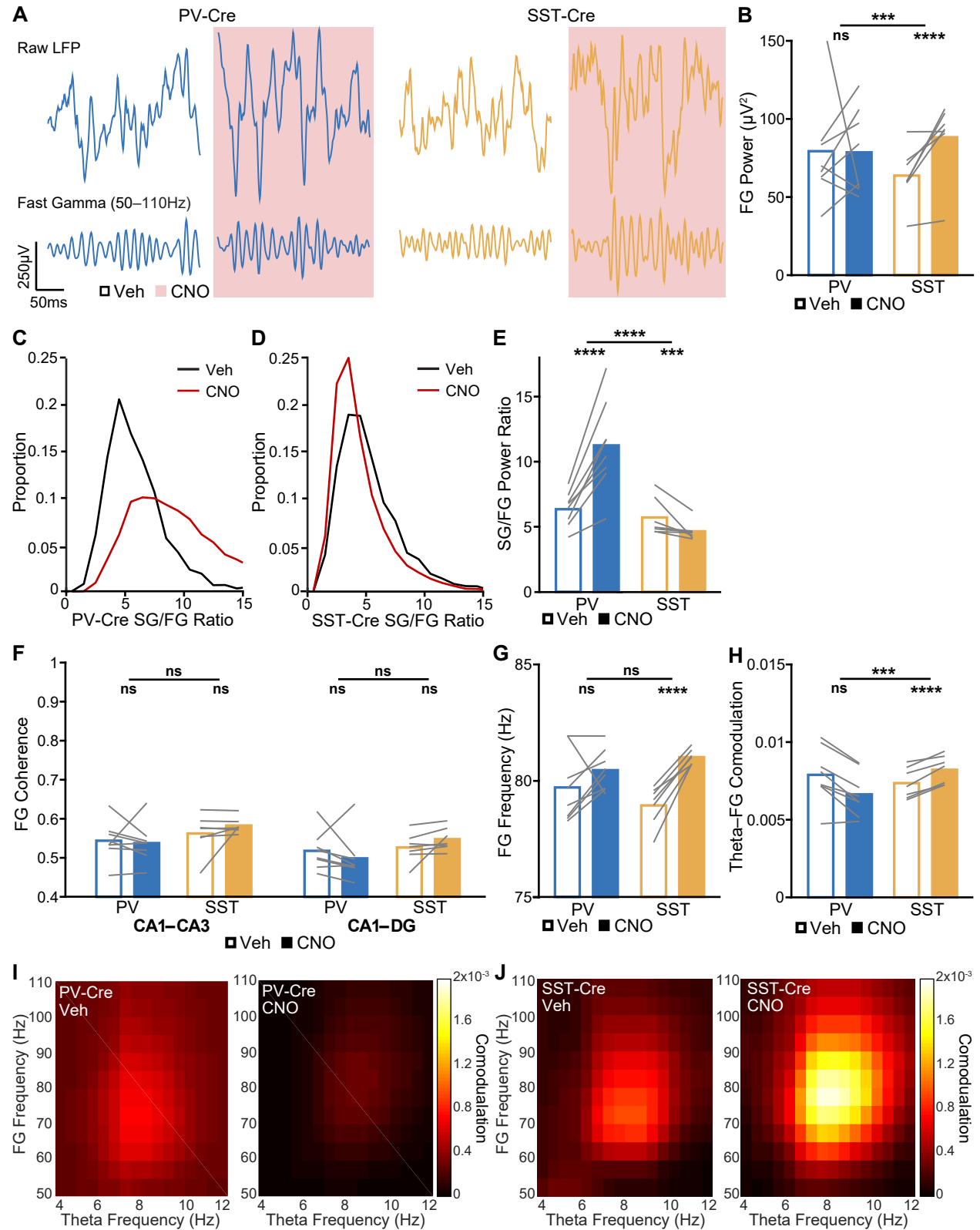
Figure 5

546 **Figure 5. Suppressing PV⁺ or SST⁺ interneurons bidirectionally modulates FG signatures of**

547 **EC coupling to CA1 during movement**.

548 (A) Example raw (top) and FG-filtered (bottom) LFP traces from CA1 pyramidal layer sites from

549 a PV-Cre (left) and an SST-Cre (right) mouse.

550 (B) FG power (PV: $p = 0.27$; SST: $p = 3.3 \times 10^{-5}$; PV vs SST: $p = 0.00054$).

551 (C,D) Representative distributions of SG/FG power ratios over 1 s bins in (C) a PV-Cre mouse

552 and (D) an SST-Cre mouse.

553 (E) Ratio of SG power to FG power (PV: $p = 9.7 \times 10^{-25}$; SST: $p = 0.00013$; PV vs SST: $p = 7.4 \times 10^{-6}$).

554

555 (F) FG frequency band coherence between CA1 and CA3 (PV: $p = 0.83$; SST: $p = 0.2$; PV vs SST:

556 $p = 0.24$) and between CA1 and DG (PV: $p = 0.27$; SST: $p = 0.076$; PV vs SST: $p = 0.47$).

557 (G) FG instantaneous frequency (PV: $p = 0.06$; SST: $p = 4.3 \times 10^{-17}$; PV vs SST: $p = 0.065$).

558 (H) Theta modulation of FG power (PV: $p = 0.0098$; SST: $p = 8 \times 10^{-20}$; PV vs SST: $p = 0.0001$).

559 (I,J) Representative comodulograms during vehicle-treated epochs (left) and CNO-treated epochs

560 (right) in a (I) a PV-Cre mouse and (J) an SST-Cre mouse.

561 N = 8 PV-Cre and n = 7 SST-Cre mice. Statistical details in Table S2. F test of the LMM for

562 treatment effects, likelihood ratio test for genotype-treatment interaction effects. **$p < 0.01$; ***p

563 < 0.001; ****$p < 0.0001$. Central values are means and individual points are mean per animal. See

564 also Figures S3, S4, and 6 and Tables S2–S6.

565

566

567

Figure 6

Suppress PV+ Interneurons

Greater CA3 drive, lower EC drive

Suppress SST+ Interneurons

Lower CA3 drive, greater EC drive

Rest

↑SWR rate
↑SWR frequency
↑SW amplitude
↑SG power during SWRs
↑SG coherence during SWRs

↓SWR rate
↑SWR length

Run

↑SG power
↑SG coherence
↑SG coupling to theta in CA3/DG
↓FG coupling to theta
↓FG coupling to theta in CA3/DG

↓SG power in CA3/DG
↓SG coupling to theta
↑FG power
↑FG coupling to theta
↑FG frequency
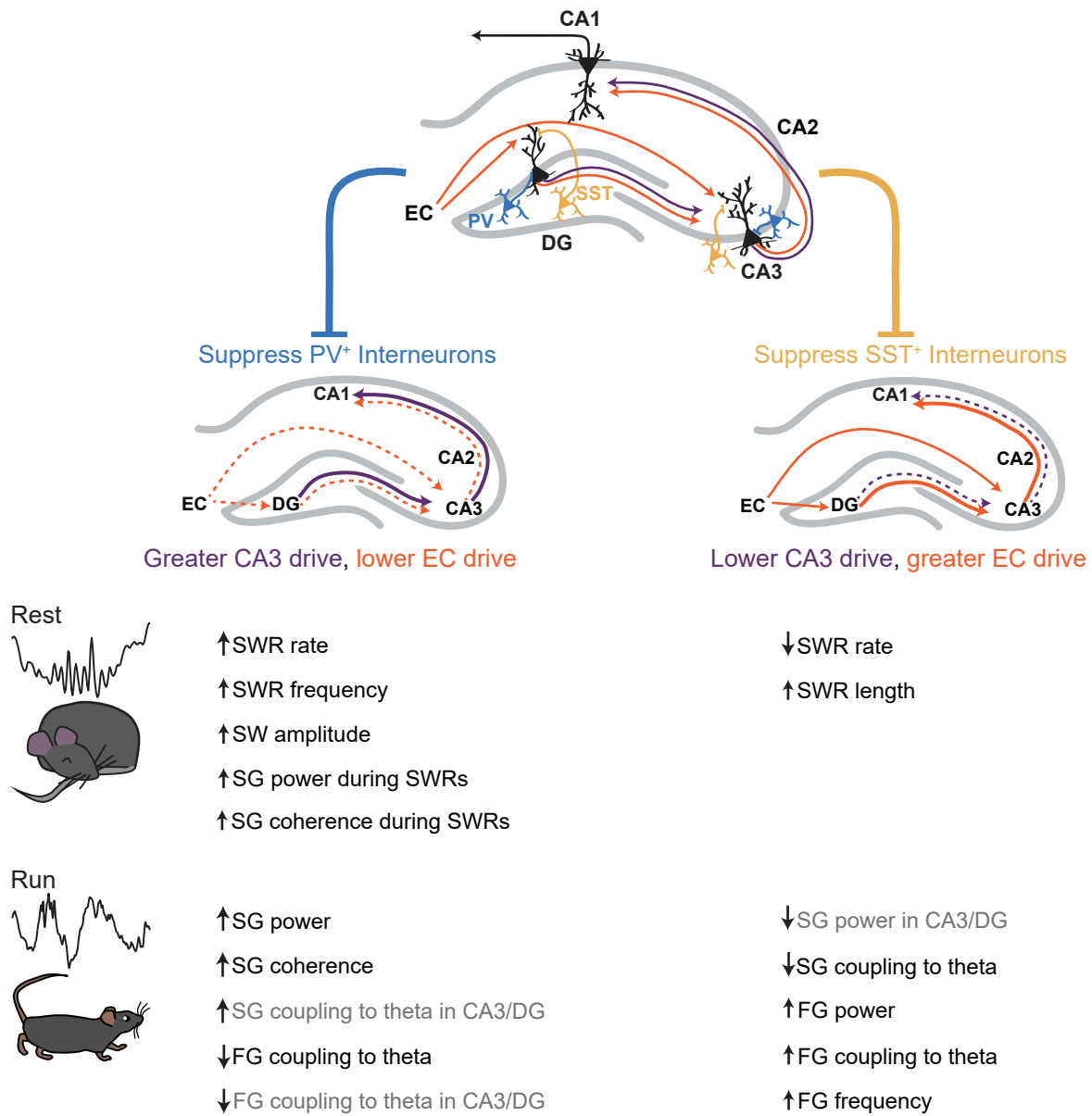
568 **Figure 6. PV+ and SST+ interneurons in DG and CA3 bidirectionally modulate signatures of**

569 **internal and external drive.**

570 CA1 receives direct input from CA3 and indirect input from DG via CA3, and these regions in

571 turn receive projections from EC layer II. PV+ (blue) and SST+ (yellow) interneurons in DG and

572 CA3 appear to regulate the switch between greater CA3 drive to CA1 and greater EC drive to CA1.

573 When PV+ interneurons are suppressed, signatures of CA3 drive are enhanced and signatures of

574 EC drive are curtailed. When SST+ interneurons are suppressed, signatures of CA3 drive are

575 curtailed and signatures of EC drive are enhanced. These manifest as changes to SWR, SW, and

576 SG properties during rest periods and to theta, SG, and FG during running periods both

577 downstream in CA1 (black) or locally in DG and CA3 (grey). These interneurons may contribute

578 to the modulation between these internal and external inputs to modulate memory representations.

579

580

581

582

583

584

585

586

587

588

589
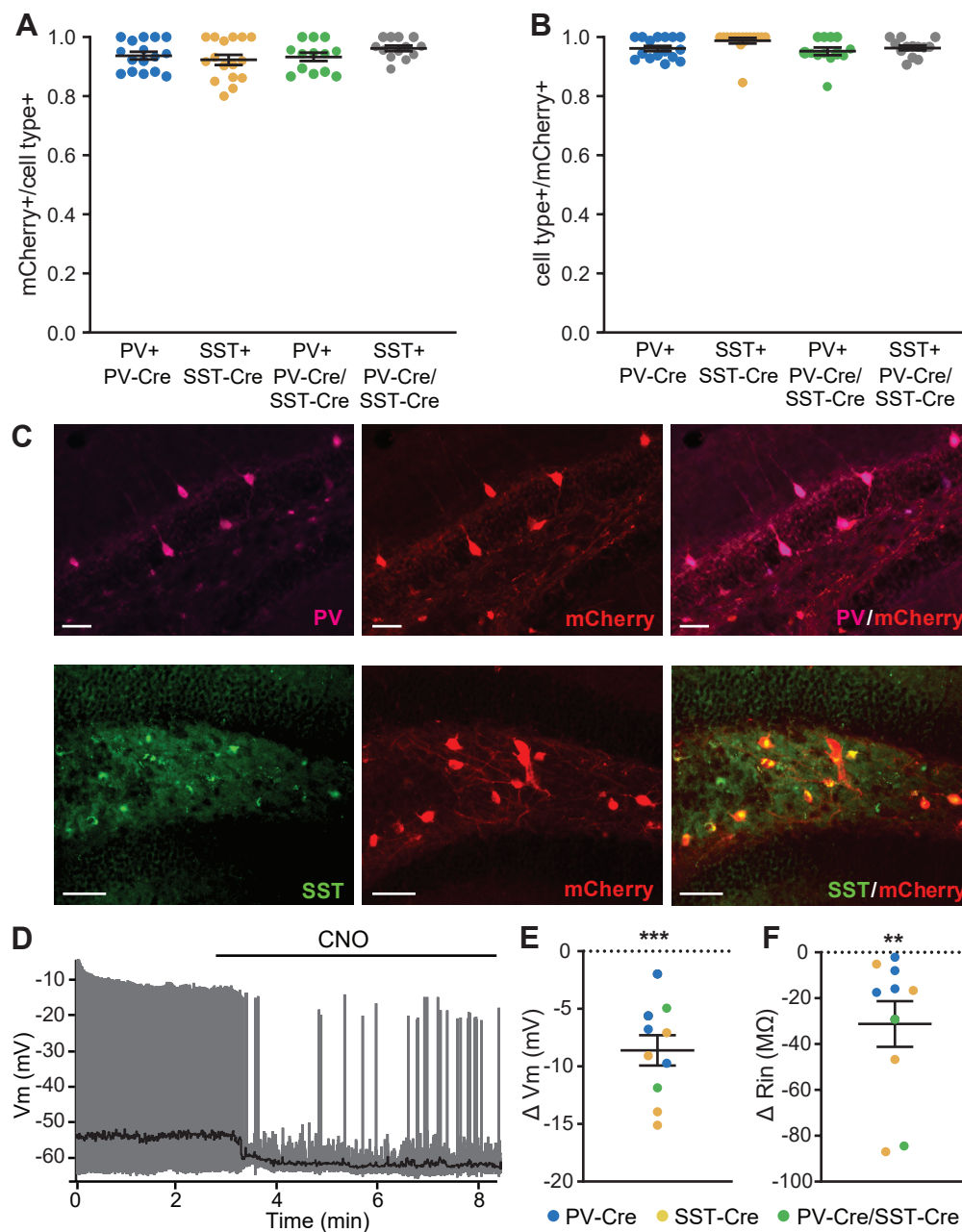
Figure S1

590 **Figure S1. DREADDs function and expression in PV$^+$ and SST$^+$ interneurons in DG and**

591 **CA3. Related to Figure 1.**

592 (A, B) Proportion of (A) mCherry$^+$ cells in PV$^+$ and SST$^+$ cells and (B) PV$^+$ and SST$^+$ cells in

593 mCherry$^+$ cells. N = 16 PV-Cre mice, n = 16 SST-Cre mice, and n = 13 PV-Cre/SST-Cre mice.

594 (C) Example of mCherry coexpression with PV (top) and SST (bottom) in DG. Scale bars are 50

595 µm.

596 (D) CNO application to *ex vivo* hippocampal sections from a PV-Cre animal reduces the firing rate

597 and resting membrane potential (black trace) of a PV$^+$ interneuron expressing hM4D.

598 (E,F) CNO application to *ex vivo* hippocampal section with PV$^+$ and SST$^+$ interneurons expressing

599 hM4D (D) hyperpolarizes cells (1-sample t test, t(9)=6.57, p = 0.0001) and (E) increases input

600 resistance (1-sample Wilcoxon test, W = -55, p = 0.002). N = 4 PV-Cre slices, n = 4 SST-Cre

601 slices, and n = 2 PV-Cre/SST-Cre slices.

602 Error bars are mean ± SEM. ***p < 0.001.

603

604

605

606

607

608

609

610

611
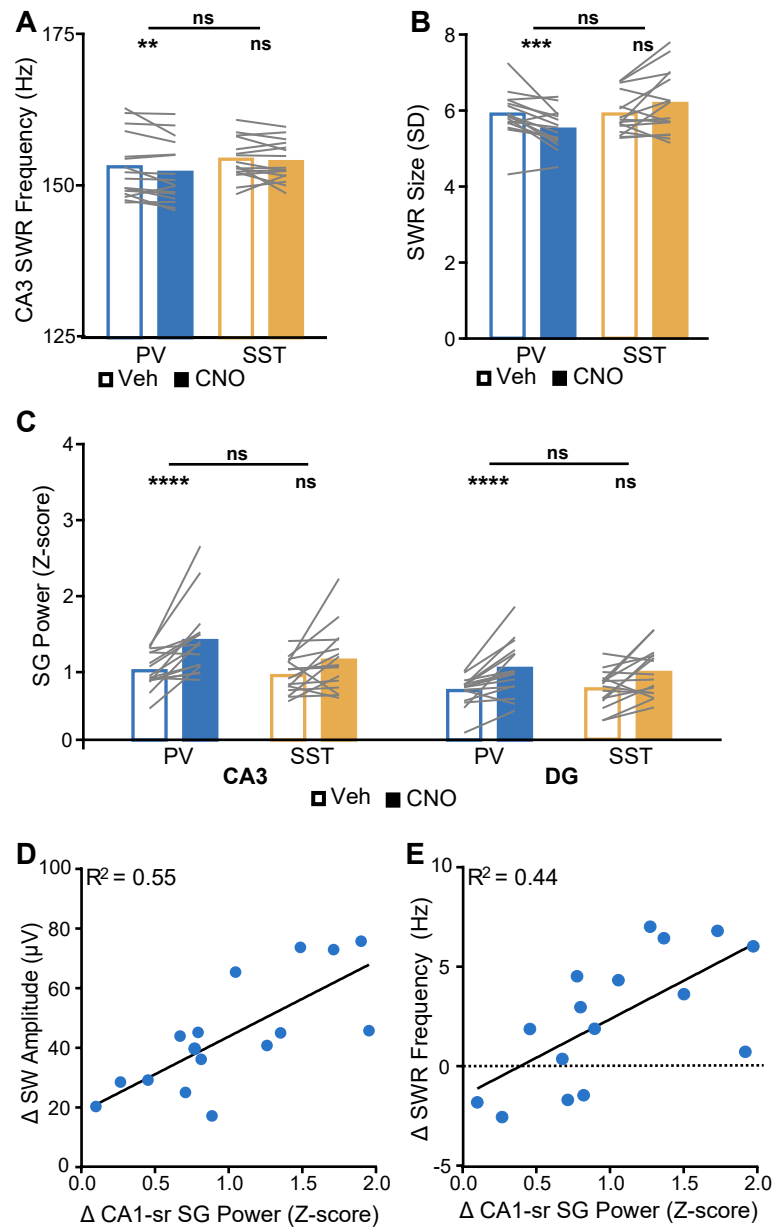
Figure S2

612 **Figure S2. Additional properties of SWRs during interneuron suppression. Related to**

613 **Figures 2 and 3.**

614 (A) SWR instantaneous frequency in CA3 (PV: $p = 0.0032$; SST: $p = 0.45$; PV vs SST: $p = 0.47$).

615 (B) SWR size (PV: $p = 0.00048$; SST: $p = 0.07$; PV vs SST: $p = 0.011$).

616 (C) Normalized SG power during SWRs in CA3 (PV: $p = 2 \times 10^{-5}$; SST: $p = 0.068$; PV vs SST: $p =$

617 0.96) and DG (PV: $p = 2.2 \times 10^{-5}$; SST: $p = 0.0058$; PV vs SST: $p = 0.95$).

618 (D,E) Change SWR-coincident SG power in CA1 in PV-Cre animals upon CNO treatment predicts

619 (D) change in SW amplitude ($F(1,14) = 17.29$, $p = 0.001$) and (E) change in SWR frequency

620 ($F(1,14) = 10.97$, $p = 0.0051$). Pearson correlation.

621 N = 16 PV-Cre and n = 16 SST-Cre mice. Statistical details in Table S2. F test of the LMM for

622 treatment effects, likelihood ratio test for genotype-treatment interaction effects. **$p < 0.01$; ***p

623 < 0.001; ****$p < 0.0001$. See also Tables S1–S6.

624

625

626

627

628

629

630

631

632

633
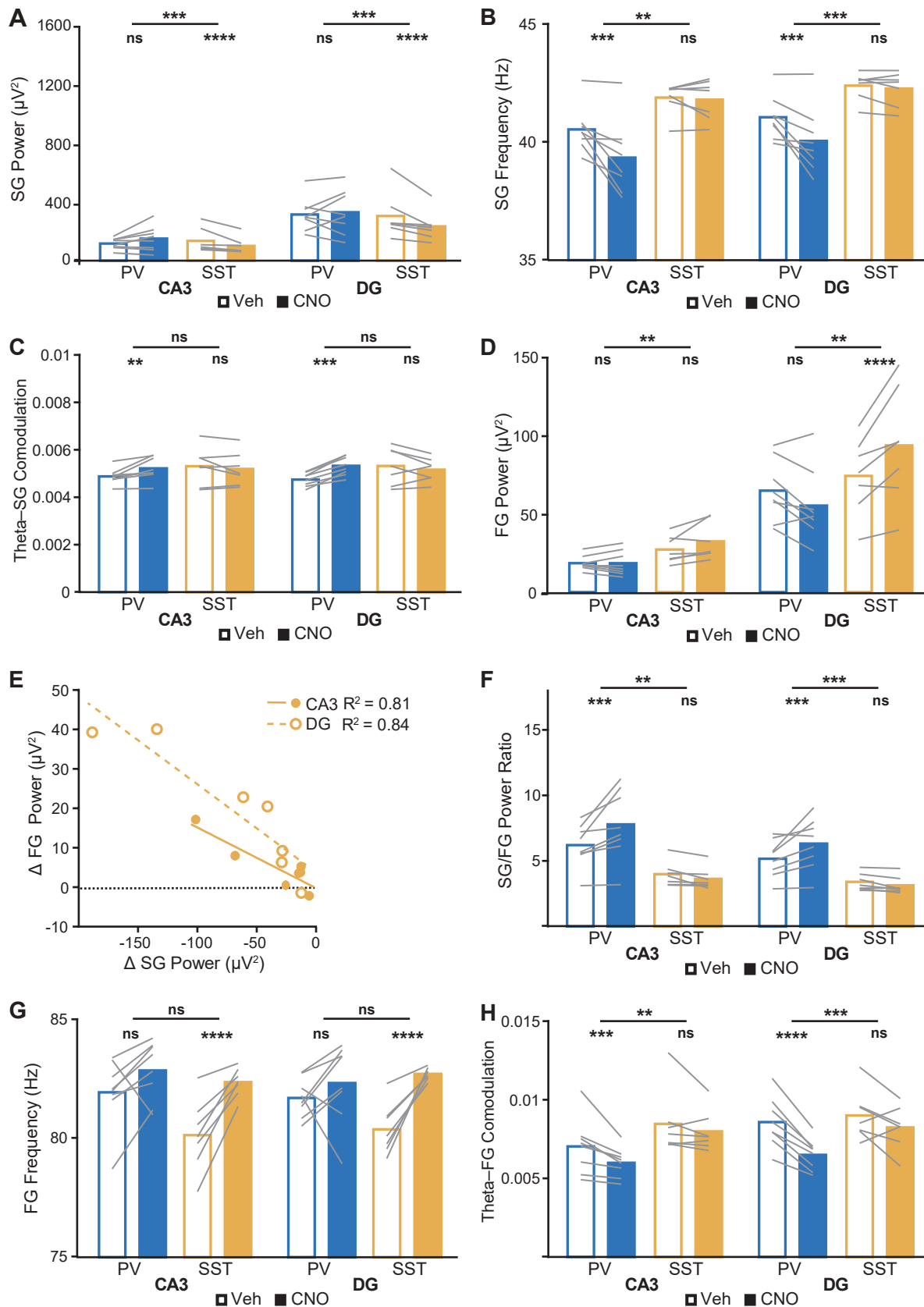
Figure S3

634 **Figure S3. Properties of SG and FG in DG and CA3 during interneuron suppression. Related**

635 **to Figures 4 and 5.**

636 (A) SG power in CA3 (PV: p = 0.15; SST: p = 5.2×10^{-5}; PV vs SST: p = 0.00088) and DG (PV: p

637 = 0.5; SST: p = 1.3×10^{-7}; PV vs SST: p = 0.00042).

638 (B) SG instantaneous frequency in CA3 (PV: p = 0.00023; SST: p = 0.8; PV vs SST: p = 0.0025)

639 and DG (PV: p = 0.0005; SST: p = 0.37; PV vs SST: p = 0.00015).

640 (C) Theta modulation of SG power in CA3 (PV: p = 0.0011; SST: p = 0.16; PV vs SST: p = 0.0049)

641 and DG (PV: p = 0.0003; SST: p = 0.22; PV vs SST: p = 0.0054).

642 (D) FG power in CA3 (PV: p = 0.42; SST: p = 0.0076; PV vs SST: p = 0.0027) and DG (PV: p =

643 0.81; SST: p = 1.9×10^{-5}; PV vs SST: p = 0.0025).

644 (E) Change in SG power in SST-Cre animals upon CNO treatment predicts change in FG power

645 in CA3 ($F(1,5) = 20.7$, p = 0.0061) and DG ($F(1,5) = 26$, p = 0.0038). Pearson correlation.

646 (F) Ratio of SG power to FG power in CA3 (PV: p = 0.00036; SST: p = 0.0071; PV vs SST: p =

647 0.002) and DG (PV: p = 0.00031; SST: p = 0.002; PV vs SST: p = 0.00064).

648 (G) FG instantaneous frequency in CA3 (PV: p = 0.02; SST: p = 2.6×10^{-9}; PV vs SST: p = 0.12)

649 and DG (PV: p = 0.23; SST: p = 4.1×10^{-11}; PV vs SST: p = 0.062).

650 (H) Theta modulation of FG power in CA3 (PV: p = 0.00041; SST: p = 0.19; PV vs SST: p =

651 0.0026) and DG (PV: p = 7.5×10^{-11}; SST: p = 0.11; PV vs SST: p = 0.00053).

652 N = 8 PV-Cre and n = 7 SST-Cre mice. Statistical details in Table S2. F test of the LMM for

653 treatment effects, likelihood ratio test for genotype-treatment interaction effects. **p < 0.01; ***p

654 < 0.001; ****p < 0.0001. Central values are means and individual points are mean per animal. See

655 also Tables S2–S6.

656
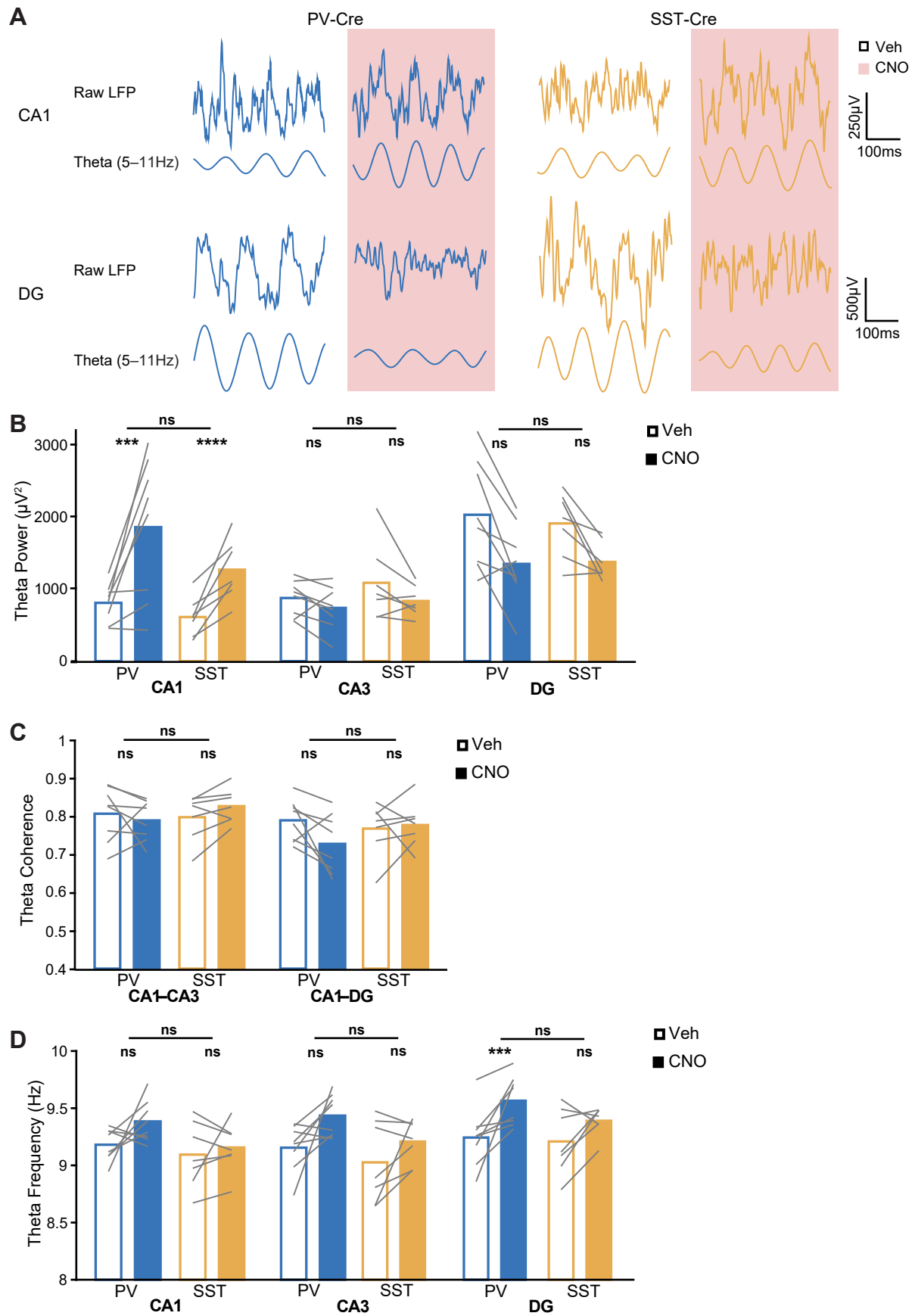
Figure S4

657   **Figure S4. Suppressing PV⁺ or SST⁺ interneurons unidirectionally modulates theta during**

658   **movement. Related to Figures 4 and 5.**

659   (A) Example raw and theta-filtered LFP traces from CA1 pyramidal layer (top) and DG granule

660   cell layer (bottom) sites from a PV-Cre (left) and an SST-Cre (right) mouse.

661   (B) Theta power in CA1 (PV: $p = 0.00032$; SST: $p = 4.2 \times 10^{-5}$; PV vs SST: $p = 0.52$), CA3 (PV: p

662   $= 0.81$; SST: $p = 0.13$; PV vs SST: $p = 0.3$), and DG (PV: $p = 0.12$; SST: $p = 0.0097$; PV vs SST:

663   $p = 0.85$).

664   (C) Theta frequency band coherence between CA1 and CA3 (PV: $p = 0.57$; SST: $p = 0.047$; PV

665   vs SST: $p = 0.62$) and between CA1 and DG (PV: $p = 0.024$; SST: $p = 0.76$; PV vs SST: $p = 0.89$).

666   (D) Theta instantaneous frequency in CA1 (PV: $p = 0.0082$; SST: $p = 0.29$; PV vs SST: $p = 0.06$),

667   CA3 (PV: $p = 0.0077$; SST: $p = 0.1$; PV vs SST: $p = 0.3$), and DG (PV: $p = 0.00061$; SST: $p = 0.1$;

668   PV vs SST: $p = 0.67$).

669   N = 8 PV-Cre and n = 7 SST-Cre mice. Statistical details in Table S2. F test of the LMM for

670   treatment effects, likelihood ratio test for genotype-treatment interaction effects. $**p < 0.01$; $***p$

671   < 0.001; $****p < 0.0001$. Central values are means and individual points are mean per animal. See

672   also Tables S2–S6.

673

674

675

676

677

678
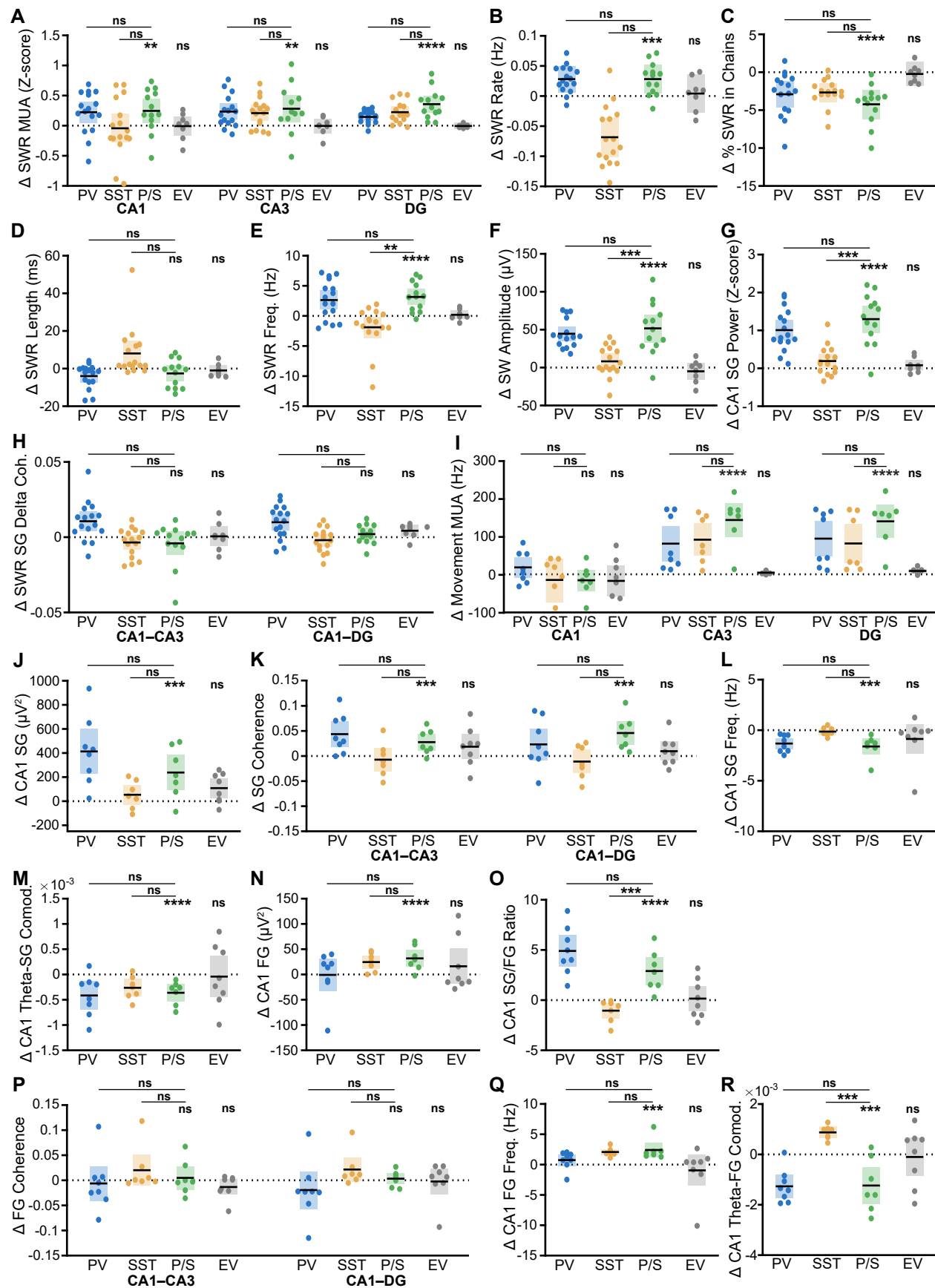
Figure S5

679 **Figure S5. Suppressing both PV$^+$ and SST$^+$ interneurons increases CA3 coupling onto CA1.**

680 **Related to Figures 2–5 and S2–S4.**

681 (A) Normalized recruitment to SWRs of MUA in CA1 (P/S: $p = 0.0074$; PV vs P/S: $p = 1$; SST vs

682 P/S: $p = 1$; EV: $p = 0.89$), CA3 (P/S: $p = 0.0053$; PV vs P/S: $p = 1$; SST vs P/S: $p = 1$; EV: $p =$

683 0.66), and DG (P/S: $p = 9 \times 10^{-7}$; PV vs P/S: $p = 1$; SST vs P/S: $p = 1$; EV: $p = 0.23$).

684 (B) SWR rate (PV-Cre/SST-Cre (P/S): $p = 0.00035$; PV vs P/S: $p = 0.87$; SST vs P/S: $p = 0.021$;

685 Empty Vector (EV): $p = 0.74$).

686 (C) Percent of SWRs following another SWR within 200 ms (P/S: $p = 1.4 \times 10^{-5}$; PV vs P/S: $p = 1$;

687 SST vs P/S: $p = 0.82$; EV: $p = 0.77$).

688 (D) SWR length (P/S: $p = 0.49$; PV vs P/S: $p = 0.8$; SST vs P/S: $p = 0.089$; EV: $p = 0.68$).

689 (E) SWR instantaneous frequency (P/S: $p = 4.2 \times 10^{-6}$; PV vs P/S: $p = 0.2$; SST vs P/S: $p = 0.0017$;

690 EV: $p = 0.62$).

691 (F) SW amplitude (P/S: $p = 5.2 \times 10^{-8}$; PV vs P/S: $p = 0.066$; SST vs P/S: $p = 0.00055$; EV: $p =$

692 0.47).

693 (G) Normalized SG power during SWRs in CA1 (P/S: $p = 8.6 \times 10^{-12}$; PV vs P/S: $p = 1$; SST vs P/S:

694 $p = 0.00089$; EV: $p = 0.13$).

695 (H) Increase during SWRs of SG frequency band coherence between CA1 and CA3 (P/S: $p = 0.32$;

696 PV vs P/S: $p = 1$; SST vs P/S: $p = 1$; EV: $p = 0.89$ and between CA1 and DG (P/S: $p = 0.23$; PV

697 vs P/S: $p = 1$; SST vs P/S: $p = 1$; EV: $p = 0.13$).

698 In A–H, n = 16 PV-Cre, n = 16 SST-Cre, n = 13 PV-Cre/SST-Cre and n = 8 empty vector mice.

699 (I) MUA during movement in CA1 (P/S: $p = 0.033$; PV vs P/S: $p = 0.98$; SST vs P/S: $p = 0.15$;

700 EV: $p = 0.23$), CA3 (P/S: $p = 1.1 \times 10^{-9}$; PV vs P/S: $p = 0.51$; SST vs P/S: $p = 0.89$; EV: $p = 0.36$),

701 and DG (P/S: $p = 1.2 \times 10^{-9}$; PV vs P/S: $p = 0.43$; SST vs P/S: $p = 0.031$; EV: $p = 0.6$).

702   (J) SG power (P/S: p = 0.00065; PV vs P/S: p = 0.78; SST vs P/S: p = 0.73; EV: p = 0.067).

703   (K) SG frequency band coherence between CA1 and CA3 (P/S: p = 0.00058; PV vs P/S: p = 0.6;

704   SST vs P/S: p = 0.45; EV: p = 0.13) and between CA1 and DG (P/S: p = 0.00098; PV vs P/S: p =

705   0.95; SST vs P/S: p = 0.26; EV: p = 0.3).

706   (L) SG instantaneous frequency (P/S: p = 0.0001; PV vs P/S: p = 0.95; SST vs P/S: p = 0.036; EV:

707   p = 0.28).

708   (M) Theta modulation of SG power (P/S: p = 7.2×10^{-7}; PV vs P/S: p = 0.66; SST vs P/S: p = 0.93;

709   EV: p = 0.87).

710   (N) FG power (P/S: p = 1.6×10^{-6}; PV vs P/S: p = 0.05; SST vs P/S: p = 1; EV: p = 0.71).

711   (O) Ratio of SG power to FG power (P/S: p = 3.8×10^{-6}; PV vs P/S: p = 0.5; SST vs P/S: p =

712   0.00086; EV: p = 0.92).

713   (P) FG frequency band coherence between CA1 and CA3 (P/S: p = 0.68; PV vs P/S: p = 0.54; SST

714   vs P/S: p = 0.1; EV: p = 0.1) and between CA1 and DG (P/S: p = 0.68; PV vs P/S: p = 0.13; SST

715   vs P/S: p = 0.16; EV: p = 0.82).

716   (Q) FG instantaneous frequency (P/S: p = 0.00012; PV vs P/S: p = 0.51; SST vs P/S: p = 0.0056;

717   EV: p = 0.44).

718   (R) Theta modulation of FG power (P/S: p = 0.00019; PV vs P/S: p = 0.53; SST vs P/S: p =

719   0.00017; EV: p = 0.91).

720   In I–R, n = 8 PV-Cre, n = 7 SST-Cre, n = 7 PV-Cre/SST-Cre and n = 8 empty vector mice.

721   Statistical details in Table S4. F test of the LMM for treatment effects, likelihood ratio test for

722   genotype-treatment interaction effects. **p < 0.01; ***p < 0.001; ****p < 0.0001. Central values

723   are LMM fixed effect coefficients β ± 95% confidence intervals and individual points are the fitted

724   conditional response for each mouse. See also Figures S5 and Table S4.

Figure S6
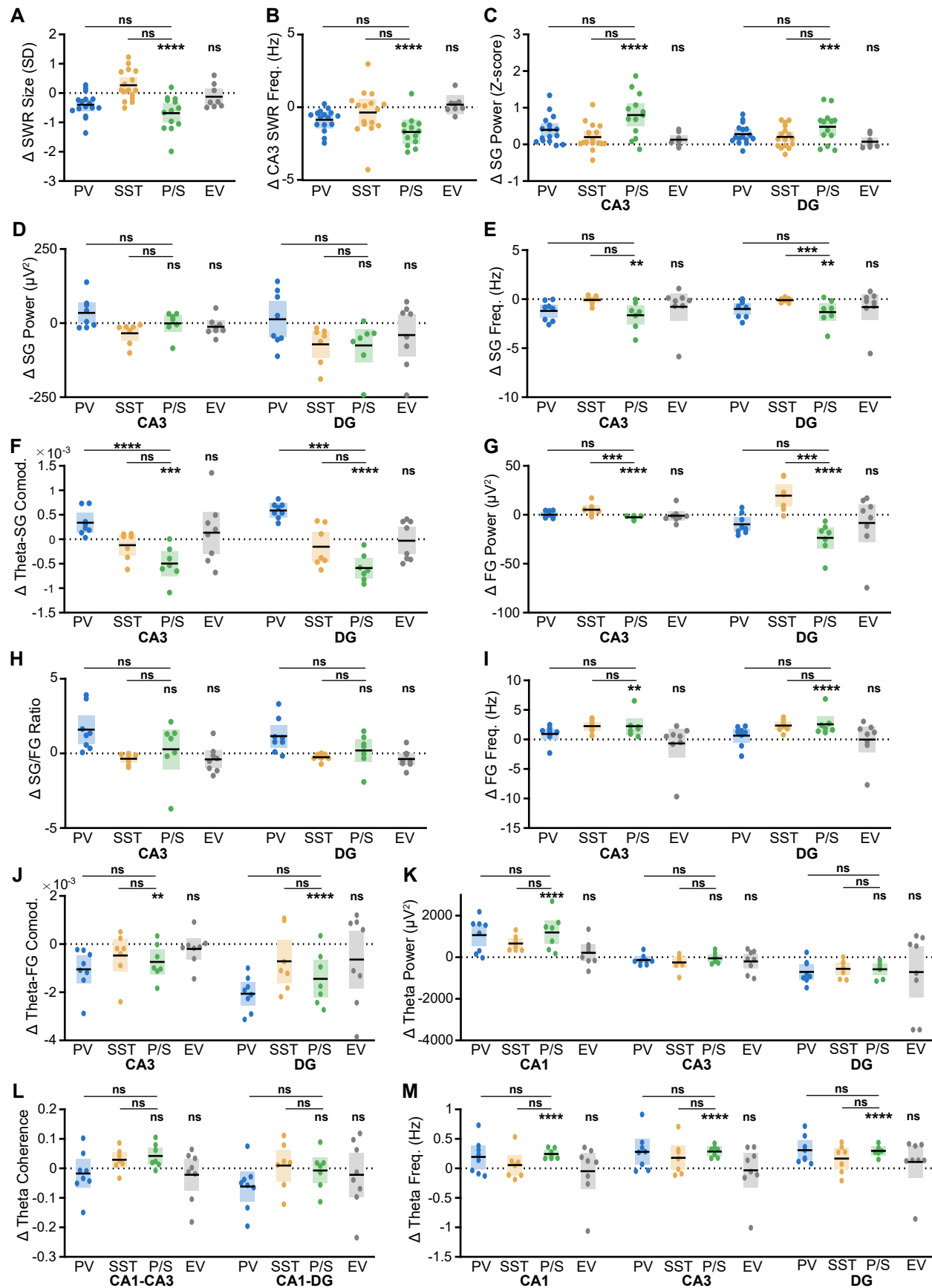
Figure S6. Additional properties demonstrating suppressing both PV$^+$ and SST$^+$ interneurons increases CA3 coupling onto CA1. Figures 2–5 and S2–S4.

(A) SWR size (PV-Cre/SST-Cre (P/S): p = 7.2x10^{-6}; PV vs P/S: p = 0.56; SST vs P/S: p = 0.031; Empty Vector (EV): p = 0.48).

(B) SWR instantaneous frequency in CA3 (P/S: p = 4.3x10^{-5}; PV vs P/S: p = 0.9; SST vs P/S: p = 0.45; EV: p = 0.53).

(C) Normalized SG power during SWRs in CA3 (P/S: p = 1.1x10^{-6}; PV vs P/S: p = 1; SST vs P/S: p = 1; EV: p = 0.062) and DG (P/S: p = 0.00013; PV vs P/S: p = 1; SST vs P/S: p = 1; EV: p = 0.22).

In A–C, n = 16 PV-Cre, n = 16 SST-Cre, n = 13 PV-Cre/SST-Cre and n = 8 empty vector mice.

(D) SG power in CA3 (P/S: p = 0.84; PV vs P/S: p = 0.47; SST vs P/S: p = 0.49; EV: p = 0.087) and DG (P/S: p = 0.017; PV vs P/S: p = 0.35; SST vs P/S: p = 0.69; EV: p = 0.63).

(E) SG instantaneous frequency in CA3 (P/S: p = 0.0029; PV vs P/S: p = 0.7; SST vs P/S: p = 0.012; EV: p = 0.32) and DG (P/S: p = 0.0045; PV vs P/S: p = 0.8; SST vs P/S: p = 0.00055; EV: p = 0.27).

(F) Theta modulation of SG power in CA3 (P/S: p = 0.00036; PV vs P/S: p = 7.3x10^{-5}; SST vs P/S: p = 0.0048; EV: p = 0.63) and DG (P/S: p = 8.4x10^{-11}; PV vs P/S: p = 0.00018; SST vs P/S: p = 0.28; EV: p = 1).

(G) FG power in CA3 (P/S: p = 2x10^{-6}; PV vs P/S: p = 0.037; SST vs P/S: p = 0.00023; EV: p = 0.36) and DG (P/S: p = 1x10^{-10}; PV vs P/S: p = 0.018; SST vs P/S: p = 0.00019; EV: p = 0.64).

(H) Ratio of SG power to FG power in CA3 (P/S: p = 0.39; PV vs P/S: p = 0.52; SST vs P/S: p = 0.022; EV: p = 0.23) and DG (P/S: p = 0.29; PV vs P/S: p = 0.66; SST vs P/S: p = 0.012; EV: p = 0.15).

748   (I) FG instantaneous frequency in CA3 (P/S: p = 0.0013; PV vs P/S: p = 0.39; SST vs P/S: p =

749   0.092; EV: p = 0.51) and DG (P/S: p = 8.6×10^{-5}; PV vs P/S: p = 0.061; SST vs P/S: p = 0.0089;

750   EV: p = 0.74).

751   (J) Theta modulation of FG power in CA3 (P/S: p = 0.0024; PV vs P/S: p = 0.68; SST vs P/S: p =

752   0.79; EV: p = 0.22) and DG (P/S: p = 8.6×10^{-5}; PV vs P/S: p = 0.75; SST vs P/S: p = 0.96; EV: p

753   = 0.35).

754   (K) Theta power in CA1 (P/S: p = 2.8×10^{-8}; PV vs P/S: p = 0.69; SST vs P/S: p = 0.51; EV: p =

755   0.1), CA3 (P/S: p = 0.35; PV vs P/S: p = 0.004; SST vs P/S: p = 0.018; EV: p = 0.67), and DG

756   (P/S: p = 0.014; PV vs P/S: p = 0.013; SST vs P/S: p = 0.028; EV: p = 0.61).

757   (L) Theta frequency band coherence between CA1 and CA3 (P/S: p = 0.0064; PV vs P/S: p = 0.66;

758   SST vs P/S: p = 1; EV: p = 0.36) and between CA1 and DG (P/S: p = 0.66; PV vs P/S: p = 0.9;

759   SST vs P/S: p = 0.91; EV: p = 0.59).

760   (M) Theta instantaneous frequency in CA1 (P/S: p = 1.4×10^{-8}; PV vs P/S: p = 0.056; SST vs P/S:

761   p = 0.55; EV: p = 0.68), CA3 (P/S: p = 5.7×10^{-8}; PV vs P/S: p = 0.16; SST vs P/S: p = 0.86; EV:

762   p = 0.74), and DG (P/S: p = 9.4×10^{-12}; PV vs P/S: p = 0.69; SST vs P/S: p = 0.54; EV: p = 0.8).

763   In D–M, n = 8 PV-Cre, n = 7 SST-Cre, n = 7 PV-Cre/SST-Cre and n = 8 empty vector mice.

764   Statistical details in Table S4. F test of the LMM for treatment effects, likelihood ratio test for

765   genotype-treatment interaction effects. **p < 0.01; ***p < 0.001; ****p < 0.0001. Central values

766   are LMM fixed effect coefficients β ± 95% confidence intervals and individual points are the fitted

767   conditional response for each mouse. See also Table S4.

768

769

770 **Table S1. Effects of suppressing PV$^+$ or SST$^+$ interneurons on SWR and SG detection.**

771 **Related to Figures 2, 3, and S2.**

Feature	Layer	Genotype	Veh. Mean	CNO Mean	statistic	df	test value	p
Ripple Freq. Mean (μV)	CA1-pyr	PV-Cre	72.39	70.96	Z	NA	1.6	0.1
		SST-Cre	61.53	58.67	Z	NA	1.24	0.2
Ripple Freq. SD (μV)	CA1-pyr	PV-Cre	77.3	76.69	t	15	0.32	0.8
		SST-Cre	64.04	65.76	t	15	0.66	0.5
Fast Ripple Rate (Hz)	CA1-pyr	**PV-Cre**	**0.0004**	**0.0035**	**Z**	**NA**	**2.93**	**0.003**
		SST-Cre	0.0015	0.0013	Z	NA	1.17	0.2
Rest MUA (Hz)	CA1-pyr	PV-Cre	10.61	10.91	Z	NA	-0.41	0.68
		SST-Cre	12.28	11.49	Z	NA	-0.16	0.88
	CA3-pyr	PV-Cre	8.1	7.4	Z	NA	1.71	0.09
		SST-Cre	6.58	5.75	Z	NA	1.6	0.11
	DG-gc	PV-Cre	7.05	6.51	Z	NA	0.98	0.33
		SST-Cre	5.78	5.91	Z	NA	0.21	0.84
Rest SG Freq. Mean (μV^2)	CA1-sr	**PV-Cre**	**109.51**	**127.6**	**t**	**15**	**4.03**	**0.001**
		SST-Cre	114.49	104.57	t	15	1.8	0.09
	CA3	PV-Cre	152.26	157.61	t	15	1.49	0.2
		SST-Cre	140	138.21	t	15	0.6	0.6
	DG	PV-Cre	353.58	352.37	t	15	0.15	0.9
		SST-Cre	338	338.89	t	15	0.1	0.94
Rest SG Freq. SD (μV^2)	CA1-sr	**PV-Cre**	**109.06**	**226.98**	**Z**	**NA**	**3.52**	**0.0004**
		SST-Cre	130.07	130.39	t	15	0.1	0.96
	CA3	**PV-Cre**	**161.1**	**252.93**	**t**	**15**	**3.94**	**0.001**
		SST-Cre	158.63	180.56	Z	NA	1.4	0.16
	DG	**PV-Cre**	**343.52**	**450.84**	**t**	**15**	**3.47**	**0.003**
		SST-Cre	355.87	382.82	t	15	1.4	0.19

772 Paired t tests when the test statistic given is t and Wilcoxon matched pairs signed rank test when

773 the test statistic given is Z. Significant comparisons are bolded. N = 16 PV-Cre and n = 16 SST-

774 Cre mice.

775

776

777

778   **Table S2. Statistical details for Figures 2–5 and S2–S4.**

Rest Features	PV-Cre (n = 16)		SST-Cre (n = 16)		PV-Cre vs SST-Cre	
	df	F	df	F	df	χ^2
CA1 MUA during SWRs (Z-score)	112503	2.33	124415	0.54	9	19.33
CA3 MUA during SWRs (Z-score)	112503	11.36	124415	11.33	9	14.84
DG MUA during SWRs (Z-score)	112503	20.64	124415	17.21	9	16.38
SWR Rate (Hz)	4023	22.81	4496	16.65	9	27.92
% SWR in Chains	112503	10.79	124415	17.78	9	2.32
SWR Frequency (Hz)	112503	10.48	124415	4.56	9	19.96
SWR Length (ms)	112503	4.54	124415	9.3	9	30.65
SW Amplitude (uV)	381794	115.42	428868	1.34	9	23.57
SWR CA1 SG Power (Z-score)	381794	99.81	428868	2.14	9	27.9
SWR CA1–CA3 Delta Coh.	903633	10.59	1182100	1.89	9	39.49
SWR CA1–DG Delta Coh.	843957	10.89	866644	0.61	9	24.47
CA3 SWR Frequency (Hz)	27780	8.69	38733	0.57	9	8.62
SWR Size (SD)	112503	12.2	124415	3.28	9	21.36
SWR CA3 SG Power (Z-score)	360566	18.19	453379	3.32	9	3.15
SWR DG SG Power (Z-score)	327914	17.98	317642	7.61	9	3.3
Run Features	PV-Cre (n = 8)		SST-Cre (n = 7)		PV-Cre vs SST-Cre	
	df	F	df	F	df	χ^2
CA1 MUA (Hz)	92444	0.13	145684	0.01	9	10.15
CA3 MUA (Hz)	92444	12.06	145684	7.89	9	4.55
DG MUA (Hz)	92444	13.62	145684	7.47	9	7.44
CA1 SG Power (μV^2)	31496	22.12	51582	2.33	9	41.12
CA1–CA3 SG Coh.	110477	13.23	166284	0.27	9	7.77
CA1–DG SG Coh.	116710	2.96	185217	1.07	9	11.26
CA1 SG Freq. (Hz)	1038019	22.17	1888216	0.33	9	23.06
CA1 Theta–SG Comod.	31496	2.43	51582	11.2	9	3.26
CA1 FG Power (μV^2)	31496	1.21	51582	17.24	9	29.45
CA1 SG/FG ratio	31496	105.64	51582	14.67	9	40.05
CA1–CA3 FG Coh.	105772	0.04	185217	1.66	9	11.57
CA1–DG FG Coh.	95893	1.21	166284	3.15	9	8.66
CA1 FG Freq (Hz)	2150099	3.52	3752150	70.63	9	16.11
CA1 Theta–FG Comod.	31496	6.68	51582	83.1	9	33.69
CA3 SG Power (μV^2)	34017	2.07	48268	16.36	9	28.22
DG SG Power (μV^2)	34037	0.45	49647	27.87	9	30.09
CA3 SG Freq. (Hz)	1218601	13.56	1864300	0.07	9	25.49
DG SG Freq. (Hz)	1230393	12.13	1924686	0.81	9	32.71
CA3 Theta–SG Comod.	34017	10.62	48268	1.99	9	23.64
DG Theta–SG Comod.	34037	13.1	49647	1.48	9	23.38
CA3 FG Power (μV^2)	34017	0.64	48268	7.12	9	25.22

DG FG Power (μV^2)	34037	0.06	49647	18.28	9	25.42
CA3 SG/FG ratio	34017	12.72	48268	7.24	9	26.11
DG SG/FG ratio	34037	13	49647	9.51	9	29.04
CA3 FG Freq. (Hz)	2593454	5.43	3656285	35.46	9	14.05
DG FG Freq. (Hz)	2577250	1.42	3768666	43.56	9	16.25
CA3 Theta–FG Comod.	34017	12.5	48268	1.72	9	25.31
DG Theta–FG Comod.	34037	42.41	49647	2.51	9	29.54
CA1 Theta Power (μV^2)	31496	12.96	51582	16.78	9	8.15
CA3 Theta Power (μV^2)	34017	0.06	48268	2.25	9	10.68
DG Theta Power (μV^2)	34037	2.4	49647	6.69	9	4.84
CA1–CA3 Theta Coh.	95893	0.32	166284	3.94	9	7.13
CA1–DG Theta Coh.	105772	5.11	185217	0.09	9	4.29
CA1 Theta Freq. (Hz)	308329	6.99	574674	1.13	9	16.36
CA3 Theta Freq. (Hz)	296280	7.11	416176	2.68	9	10.69
DG Theta Freq. (Hz)	297566	11.76	432042	2.68	9	6.64

779   F test of the LMM for treatment effects, likelihood ratio test for genotype-treatment interaction

780   effects.

781

782

783

784

785

786

787

788

789

790

Table S3. Differences between genotypes during vehicle treatment. Related to Figures 2–5 and S2–S4.

Rest Features	PV mean (n = 16)	SST mean (n = 16)	df	F	p
CA1 MUA during SWRs (Z-score)	2.64	1.44	138109	2.2	0.14
CA3 MUA during SWRs (Z-score)	1.89	0.88	138261	4.1	0.042
DG MUA during SWRs (Z-score)	1.74	0.51	135839	0.082	0.77
SWR Rate (Hz)	0.45	0.44	4757	1.5	0.22
% SWR in Chains	0.2	0.21	137661	0.26	0.61
SWR Length (ms)	102.99	101.34	137661	0.0073	0.93
SWR Frequency (Hz)	156.24	156.15	137661	0.0004	0.98
SW Amplitude (uV)	375.21	384.95	471767	0.13	0.72
SWR CA1 SG Power (Z-score)	1.31	1.25	471767	0.045	0.83
SWR CA1–CA3 Delta Coh.	0.013	0.011	1189551	0.19	0.66
SWR CA1–DG Delta Coh.	0.011	0.0088	976070	2.4	0.12
CA3 SWR Frequency (Hz)	153.12	154.37	38901	0.69	0.41
SWR Size (SD)	5.93	5.93	137661	0.052	0.82
SWR CA3 SG Power (Z-score)	0.91	0.85	473237	3	0.085
SWR DG SG Power (Z-score)	0.65	0.67	359153	0.29	0.59
Run Features	PV mean (n = 8)	SST mean (n = 7)	df	F	p
CA1 MUA (Hz)	87.61	136.28	155440	2.38	0.12
CA3 MUA (Hz)	283.88	216.70	155440	1.79	0.18
DG MUA (Hz)	294.51	296.34	155400	0.00	0.99
CA1 SG Power (μV^2)	512.08	400.01	28766	0.77	0.38
CA1–CA3 SG Coh.	0.6	0.6	100543	4.20×10^{-5}	0.99
CA1–DG SG Coh.	0.59	0.58	114500	0.04	0.84
CA1 SG Freq. (Hz)	40.24	41.2	1066217	4.6	0.032
CA1 Theta–SG Comod.	0.0051	0.0049	28766	0.0015	0.97
CA1 FG Power (μV^2)	79.36	63.72	28766	0.34	0.56
CA1 SG/FG ratio	6.35	5.71	28766	1	0.32
CA1–CA3 FG Coh.	0.54	0.56	110360	0.81	0.37
CA1–DG FG Coh.	0.52	0.53	95023	0.31	0.58
CA1 FG Freq (Hz)	79.7	78.93	2095627	1.3	0.25
CA1 Theta–FG Comod.	0.0079	0.0074	28766	0.036	0.85
CA3 SG Power (μV^2)	115.94	134.21	31822	1.2	0.28
DG SG Power (μV^2)	313.19	303.08	31169	0.11	0.74
CA3 SG Freq. (Hz)	**40.54**	**41.9**	**1089935**	**12**	**0.00042**
DG SG Freq. (Hz)	**41.06**	**42.4**	**1241681**	**13**	**0.00025**
CA3 Theta–SG Comod.	0.0049	0.0053	31822	2.2	0.14

DG Theta–SG Comod.	0.0047	0.0053	31169	4.5	0.034
CA3 FG Power (μV^2)	18.3	27.1	31822	5.6	0.018
DG FG Power (μV^2)	64.54	73.9	31169	2.3	0.13
CA3 SG/FG ratio	**6.2**	**3.99**	**31822**	**11**	**0.00078**
DG SG/FG ratio	**5.16**	**3.4**	**31169**	**11**	**0.00071**
CA3 FG Freq. (Hz)	81.99	80.18	2155990	5.2	0.022
DG FG Freq. (Hz)	81.75	80.42	2381526	6.7	0.0095
CA3 Theta–FG Comod.	0.007	0.0085	31822	4	0.046
DG Theta–FG Comod.	0.0086	0.009	31169	0.94	0.33
CA1 Theta Power (μV^2)	811.3	613.97	28766	0.21	0.64
CA3 Theta Power (μV^2)	878.78	1090.14	31822	2.3	0.13
DG Theta Power (μV^2)	2036.8	1927.36	31169	0.35	0.56
CA1–CA3 Theta Coh.	0.81	0.8	95023	0.046	0.83
CA1–DG Theta Coh.	0.79	0.77	110360	0.39	0.53
CA1 Theta Freq. (Hz)	9.18	9.09	312211	0.34	0.56
CA3 Theta Freq. (Hz)	9.15	9.03	246172	0.38	0.54
DG Theta Freq. (Hz)	9.24	9.21	270460	0.056	0.81

793   F test of the LMM for genotype effects. Significant comparisons are bolded.

794

795

796

797

798

799

800

801

802

803

804 **Table S4. Statistical details for Figures S5 and S6.**

Rest Features	PV-Cre/ SST-Cre (n = 13)		PV-Cre vs PV-Cre/ SST-Cre		SST-Cre vs PV-Cre/ SST-Cre		Empty Vector (n = 8)	
	df	F	df	χ^2	df	χ^2	df	F
MUA during SWRs (Z-score)	76435	7.16	9	-68724	9	-54461	21480	0.02
MUA during SWRs (Z-score)	76435	7.78	9	-49460	9	-19733	21480	0.19
MUA during SWRs (Z-score)	76435	24.13	9	-120845	9	-6232	21480	1.42
SWR Rate (Hz)	2709	12.79	9	4.51	9	19.54	892	0.11
% SWR in Chains	75927	18.82	9	1.45	9	5.19	21310	0.08
SWR Length (ms)	75927	0.48	9	5.36	9	15.06	21310	0.17
SWR Frequency (Hz)	75927	21.2	9	12.28	9	26.56	21310	0.25
SW Amplitude (uV)	255972	29.64	9	16.03	9	29.41	66351	0.52
CA1-sr SG Power (Z-score)	255972	46.62	9	-26019	9	28.18	66351	2.33
SWR Delta SG Coherence	750476	0.99	9	-40005	9	-35500	168587	0.02
SWR Delta SG Coherence	524754	1.44	9	-97130	9	-63661	142513	2.35
CA3 SWR Frequency (Hz)	21295	16.73	9	4.19	9	8.92	8004	0.4
SWR Size (SD)	75927	20.15	9	7.7	9	18.37	21310	0.49
SG Power (Z-score)	303136	23.76	9	-15146	9	-26292	84625	3.48
SG Power (Z-score)	209470	14.65	9	-5617	9	-291	68253	1.5
Run Features	PV-Cre/ SST-Cre (n = 7)		PV-Cre vs PV-Cre/ SST-Cre		SST-Cre vs PV-Cre/ SST-Cre		Empty Vector (n = 8)	
	df	F	df	χ^2	df	χ^2	df	F
CA1 MUA (Hz)	140065	4.54	9	2.69	9	13.32	120735	1.44
CA3 MUA (Hz)	140065	37.10	9	8.28	9	4.24	120735	0.85
DG MUA (Hz)	140065	36.95	9	9.11	9	18.41	120735	0.27
CA1 SG Power (μV^2)	50966	11.62	9	5.56	9	6.07	45384	3.36
CA1–CA3 SG Coh.	204656	11.84	9	7.35	9	8.89	178143	2.26
CA1–DG SG Coh.	170411	10.86	9	3.28	9	11.26	167832	1.06
CA1 SG Freq. (Hz)	1817692	15.1	9	3.34	9	17.93	1649935	1.14
CA1 Theta–SG Comod.	50966	24.58	9	6.73	9	3.76	45384	0.02
CA1 FG Power (μV^2)	50966	23.04	9	16.9	9	1.37	49047	0.13
CA1 SG/FG ratio	50966	21.37	9	8.33	9	28.28	49047	0.01
CA1–CA3 FG Coh.	170411	0.17	9	7.95	9	14.52	173082	2.64
CA1–DG FG Coh.	204656	0.17	9	13.66	9	12.98	185143	0.05
CA1 FG Freq (Hz)	3744547	14.73	9	8.25	9	23.3	3333362	0.61
CA1 Theta–FG Comod.	50966	13.94	9	7.99	9	32.4	45384	0.01
CA3 SG Power (μV^2)	58724	0.04	9	8.69	9	8.4	59762	2.92
DG SG Power (μV^2)	48576	5.71	9	9.99	9	6.48	51661	0.24
CA3 SG Freq. (Hz)	2137020	8.89	9	6.36	9	21.1	2220964	1
DG SG Freq. (Hz)	1790505	8.08	9	5.33	9	29.44	1961970	1.2

CA3 Theta–SG Comod.	58724	12.75	9	34.51	9	23.71	59762	0.23
DG Theta–SG Comod.	48576	42.17	9	32.26	9	10.98	51661	0
CA3 FG Power (μV^2)	58724	22.57	9	17.82	9	31.67	59762	0.86
DG FG Power (μV^2)	48576	41.75	9	19.95	9	32.09	51661	0.21
CA3 SG/FG ratio	58724	0.74	9	8.14	9	19.44	59762	1.42
DG SG/FG ratio	48576	1.11	9	6.75	9	21.1	51661	2.11
CA3 FG Freq. (Hz)	4425768	10.28	9	9.55	9	14.96	4511384	0.43
DG FG Freq. (Hz)	3665938	15.43	9	16.3	9	22	3911662	0.11
CA3 Theta–FG Comod.	58724	9.18	9	6.54	9	5.48	59762	1.48
DG Theta–FG Comod.	48576	15.43	9	5.86	9	3.03	51661	0.88
CA1 Theta Power (μV^2)	50966	30.84	9	6.49	9	8.21	49047	2.7
CA3 Theta Power (μV^2)	58724	0.86	9	24.22	9	20.06	59762	0.18
DG Theta Power (μV^2)	48576	6.03	9	20.96	9	18.68	51661	0.26
CA1–CA3 Theta Coh.	204656	7.44	9	6.77	9	1.07	185143	0.84
CA1–DG Theta Coh.	170411	0.19	9	4.17	9	3.98	173082	0.29
CA1 Theta Freq. (Hz)	529462	32.2	9	16.59	9	7.85	473424	0.17
CA3 Theta Freq. (Hz)	508905	29.47	9	13.03	9	4.72	513283	0.11
DG Theta Freq. (Hz)	421267	46.45	9	6.52	9	7.92	451191	0.06

805   F test of the LMM for treatment effects, likelihood ratio test for genotype-treatment interaction

806   effects.

807

808

809

810

811

812

813

814

815

816

817   **Table S5. Sex differences across all mice during vehicle treatment. Related to Figures 2–6**

818   **and S2–S6.**

Rest Features	F mean (n = 26)	M mean (n = 27)	df	F	p
CA1 MUA during SWRs (Z-score)	1.97	1.86	189147	3.2	0.074
CA3 MUA during SWRs (Z-score)	1.28	1.13	189147	0.35	0.56
DG MUA during SWRs (Z-score)	0.98	0.96	189147	2.1	0.15
SWR Rate (Hz)	0.42	0.44	6724	0.89	0.34
% SWR in Chains	0.21	0.21	189147	0.16	0.69
SWR Length (ms)	101.02	102.9	189147	0.31	0.58
SWR Frequency (Hz)	155.74	155.45	189147	0.07	0.79
SW Amplitude (uV)	356.84	416.36	642232	4.6	0.032
SWR CA1 SG Power (Z-score)	1.31	1.22	642232	1.2	0.27
SWR CA1–CA3 Delta Coh.	0.01	0.01	1666279	0.16	0.69
SWR CA1–DG Delta Coh.	0.01	0.01	1323512	0.28	0.6
CA3 SWR Frequency (Hz)	154.3	153.8	55103	0.14	0.71
SWR Size (SD)	**6.36**	**5.92**	**189147**	**8**	**0.0046**
SWR CA3 SG Power (Z-score)	0.89	0.92	679511	0.51	0.48
SWR DG SG Power (Z-score)	0.66	0.69	506782	0.07	0.79
Run Features	F mean (n = 15)	M mean (n = 15)	df	F	p
CA1 MUA (Hz)	93.65	121.75	319923	0.19	0.67
CA3 MUA (Hz)	316.81	263.00	304843	4.36	0.04
DG MUA (Hz)	329.59	296.09	304803	4.32	0.04
CA1 SG Power (μV^2)	485.49	482.7	66893	0.016	0.9
CA1–CA3 SG Coh.	0.61	0.61	250460	0	0.99
CA1–DG SG Coh.	0.58	0.57	244915	0.2	0.65
CA1 SG Freq. (Hz)	40.48	40.76	2465138	0.33	0.56
CA1 Theta–SG Comod.	0	0.01	66893	2.2	0.14
CA1 FG Power (μV^2)	74.66	72.33	66893	0.36	0.55
CA1 SG/FG ratio	6.17	6.37	66893	0.35	0.55
CA1–CA3 FG Coh.	0.56	0.56	242401	0.0066	0.94
CA1–DG FG Coh.	0.53	0.53	246436	0.026	0.87
CA1 FG Freq (Hz)	79.12	78.93	4907656	0.0021	0.96
CA1 Theta–FG Comod.	0.01	0.01	66893	1.3	0.25
CA3 SG Power (μV^2)	133.15	135.51	77230	0.0069	0.93
DG SG Power (μV^2)	367.43	336.19	80834	1.1	0.3
CA3 SG Freq. (Hz)	41.03	41.11	2806688	0.034	0.85
DG SG Freq. (Hz)	41.49	41.81	2717918	0.49	0.48
CA3 Theta–SG Comod.	0.01	0.01	77230	0.22	0.64

DG Theta–SG Comod.	0.01	0.01	80834	0.62	0.43
CA3 FG Power (μV^2)	25.11	23.56	77230	0.026	0.87
DG FG Power (μV^2)	85.72	75.36	80834	0.4	0.53
CA3 SG/FG ratio	5.53	5.27	77230	0.12	0.73
DG SG/FG ratio	4.7	4.27	80834	0.64	0.42
CA3 FG Freq. (Hz)	81.24	80.63	5598054	0.27	0.6
DG FG Freq. (Hz)	80.65	80.91	5337353	0.7	0.4
CA3 Theta–FG Comod.	0.01	0.01	77230	1.3	0.26
DG Theta–FG Comod.	0.01	0.01	80834	0.16	0.69
CA1 Theta Power (μV^2)	795.65	885.27	66893	0.19	0.66
CA3 Theta Power (μV^2)	1153.66	1005.65	77230	1.1	0.29
DG Theta Power (μV^2)	2545.05	1940.38	80834	4.6	0.032
CA1–CA3 Theta Coh.	0.79	0.81	246436	0.88	0.35
CA1–DG Theta Coh.	0.78	0.77	280238	0.18	0.67
CA1 Theta Freq. (Hz)	9.16	9.13	713763	0.0071	0.93
CA3 Theta Freq. (Hz)	9.11	9.09	641545	0.12	0.73
DG Theta Freq. (Hz)	9.16	9.27	611269	0.37	0.54

819   F test of the LMM for sex effects. Significant comparisons are bolded.

820

821

822

823

824

825

826

827

828

829

830

831

832

833 **Table S6. Effects of PV$^+$ and/or SST$^+$ interneuron suppression stratified by sex. Related to**

834 **Figures 2–6 and S2–S6.**

PV-Cre: Rest Features	F β (n = 9)	M β (n = 7)	df	χ2	p
CA1 MUA during SWRs (Z-score)	0.16	0.18	9	-8406	1
CA3 MUA during SWRs (Z-score)	0.14	0.27	9	-46879	1
DG MUA during SWRs (Z-score)	0.11	0.11	9	-10142	1
SWR Rate (Hz)	0.058	0.073	9	2.3	0.99
% SWR in Chains	-0.00065	-0.00088	9	10	0.33
SWR Length (ms)	-4	-1.1	9	2.4	0.98
SWR Frequency (Hz)	2.3	3	9	1.4	1
SW Amplitude (uV)	37	37	9	2	0.99
SWR CA1 SG Power (Z-score)	0.66	0.72	9	-20193	1
SWR CA1–CA3 Delta Coh.	0.013	0.0089	9	-47795	1
SWR CA1–DG Delta Coh.	0.015	0.0038	9	-29872	1
CA3 SWR Frequency (Hz)	-1.1	-0.67	9	5.7	0.77
SWR Size (SD)	-0.29	-0.33	9	3.2	0.96
SWR CA3 SG Power (Z-score)	0.23	0.35	9	-21508	1
SWR DG SG Power (Z-score)	0.14	0.3	9	-5520	1
PV-Cre: Run Features	F β (n = 4)	M β (n = 4)	df	χ2	p
CA1 MUA (Hz)	1.23	-0.07	9	12	0.19
CA3 MUA (Hz)	**367.64**	**3.33**	**9**	**40**	**9.2x10^{-6}**
DG MUA (Hz)	**441.12**	**4.24**	**9**	**53**	**2.6x10^{-8}**
CA1 SG Power (μV^2)	458	156	9	5	0.81
CA1–CA3 SG Coh.	0.076	0.015	9	12	0.21
CA1–DG SG Coh.	0.06	-0.0086	9	25	0.0032
CA1 SG Freq. (Hz)	-1.4	-1.4	9	19	0.028
CA1 Theta–SG Comod.	0.000063	-0.00059	9	12	0.2
CA1 FG Power (μV^2)	24	8.9	9	9	0.47
CA1 SG/FG ratio	4.9	3	9	4	0.92
CA1–CA3 FG Coh.	-0.022	0.017	9	20	0.017
CA1–DG FG Coh.	-0.044	0.011	9	17	0.047
CA1 FG Freq (Hz)	0.33	1.3	9	5	0.82
CA1 Theta–FG Comod.	-0.00031	-0.0011	9	7	0.61
CA3 SG Power (μV^2)	45	8.9	9	6	0.76
DG SG Power (μV^2)	50	2.8	9	7	0.6
CA3 SG Freq. (Hz)	-1.4	-1.1	9	8	0.52
DG SG Freq. (Hz)	-1.4	-0.79	9	8	0.57
CA3 Theta–SG Comod.	0.000041	0.0004	9	11	0.3
DG Theta–SG Comod.	0.00026	0.00047	9	6	0.78

CA3 FG Power (μV^2)	5	-0.66	9	13	0.16
DG FG Power (μV^2)	1.5	-5.5	9	5	0.79
CA3 SG/FG ratio	1.8	0.74	9	11	0.3
DG SG/FG ratio	1.4	0.52	9	9	0.46
CA3 FG Freq. (Hz)	0.19	1.9	9	17	0.053
DG FG Freq. (Hz)	1	0.3	9	10	0.35
CA3 Theta–FG Comod.	-0.00016	-0.00091	9	9	0.4
DG Theta–FG Comod.	-0.0011	-0.0017	9	5	0.81
CA1 Theta Power (μV^2)	1318	202	9	14	0.14
CA3 Theta Power (μV^2)	143	-147	9	5	0.79
DG Theta Power (μV^2)	-104	-380	9	9	0.48
CA1–CA3 Theta Coh.	0.033	-0.068	9	5	0.81
CA1–DG Theta Coh.	-0.019	-0.12	9	4	0.92
CA1 Theta Freq. (Hz)	0.047	0.43	9	17	0.049
CA3 Theta Freq. (Hz)	0.075	0.5	9	24	0.0036
DG Theta Freq. (Hz)	0.15	0.53	9	25	0.0034
SST-Cre: Rest Features	F β (n = 5)	M β (n = 11)	df	χ2	p
CA1 MUA during SWRs (Z-score)	-0.14	0.042	9	-57534	1
CA3 MUA during SWRs (Z-score)	0.16	0.2	9	-3606	1
DG MUA during SWRs (Z-score)	0.12	0.17	9	-81019	1
SWR Rate (Hz)	-0.049	-0.036	9	2	0.99
% SWR in Chains	-0.0015	-0.00046	9	10	0.32
SWR Length (ms)	11	4.8	9	12	0.24
SWR Frequency (Hz)	-4.3	-0.78	9	22	0.0093
SW Amplitude (uV)	**-5.8**	**14**	**9**	**27**	**0.0016**
SWR CA1 SG Power (Z-score)	-0.092	0.19	9	-32461	1
SWR CA1–CA3 Delta Coh.	-0.012	-0.00035	9	-20181	1
SWR CA1–DG Delta Coh.	-0.0042	-0.00094	9	-83276	1
CA3 SWR Frequency (Hz)	-1.3	0.05	9	4.1	0.9
SWR Size (SD)	0.091	0.24	9	6.6	0.68
SWR CA3 SG Power (Z-score)	-0.027	0.19	9	-15984	1
SWR DG SG Power (Z-score)	0.051	0.19	9	-28517	1
SST-Cre: Run Features	F β (n = 3)	M β (n = 4)	df	χ2	p
CA1 MUA (Hz)	-18.59	1.42	9	10	0.36
CA3 MUA (Hz)	**308.17**	**2.33**	**9**	**32**	**0.00021**
DG MUA (Hz)	**437.16**	**2.59**	**9**	**39**	**$1.3x10^{-5}$**
CA1 SG Power (μV^2)	53	51	9	11	0.27
CA1–CA3 SG Coh.	-0.034	0.015	9	8	0.57
CA1–DG SG Coh.	-0.027	0.00079	9	13	0.14
CA1 SG Freq. (Hz)	0.34	-0.41	9	17	0.052
CA1 Theta–SG Comod.	$-1.30x10^{-4}$	-0.00037	9	21	0.012

CA1 FG Power (µV²)	**36**	**8.4**	**9**	**34**	**0.000086**
CA1 SG/FG ratio	-0.8	-1.2	9	13	0.18
CA1–CA3 FG Coh.	0.003	0.035	9	15	0.086
CA1–DG FG Coh.	0.013	0.026	9	20	0.016
CA1 FG Freq (Hz)	1.6	2.5	9	14	0.13
CA1 Theta–FG Comod.	0.00076	0.00068	9	11	0.25
CA3 SG Power (µV²)	-12	-36	9	18	0.03
DG SG Power (µV²)	-40	-73	9	11	0.28
CA3 SG Freq. (Hz)	0.17	-0.2	9	23	0.0052
DG SG Freq. (Hz)	0.0015	-0.15	9	17	0.055
CA3 Theta–SG Comod.	-1.30×10^{-4}	-0.00016	9	17	0.046
DG Theta–SG Comod.	-7.10×10^{-5}	-0.00021	9	5	0.87
CA3 FG Power (µV²)	2.5	5.6	9	15	0.1
DG FG Power (µV²)	17	16	9	9	0.45
CA3 SG/FG ratio	-0.062	-0.52	9	23	0.0053
DG SG/FG ratio	-0.1	-0.32	9	13	0.17
CA3 FG Freq. (Hz)	1.5	2.8	9	18	0.033
DG FG Freq. (Hz)	1.6	2.9	9	25	0.003
CA3 Theta–FG Comod.	-0.00036	-0.00022	9	12	0.22
DG Theta–FG Comod.	-0.00083	-0.00049	9	7	0.67
CA1 Theta Power (µV²)	712	204	9	16	0.061
CA3 Theta Power (µV²)	65	-372	9	6	0.73
DG Theta Power (µV²)	-114	-633	9	5	0.83
CA1–CA3 Theta Coh.	0.043	0.028	9	5	0.84
CA1–DG Theta Coh.	-0.013	0.028	9	11	0.25
CA1 Theta Freq. (Hz)	-0.1	0.25	9	22	0.0086
CA3 Theta Freq. (Hz)	-0.027	0.31	9	20	0.017
DG Theta Freq. (Hz)	0.034	0.28	9	10	0.38
PV-Cre/SST-Cre: Rest Features	F β (n = 8)	M β (n = 5)	df	χ2	p
CA1 MUA during SWRs (Z-score)	0.56	0.23	9	-10100	1
CA3 MUA during SWRs (Z-score)	0.24	0.25	9	-5390	1
DG MUA during SWRs (Z-score)	0.23	0.21	9	-33509	1
SWR Rate (Hz)	0.046	0.056	9	2.3	0.98
% SWR in Chains	-0.00085	-0.0013	9	6.2	0.72
SWR Length (ms)	0.21	-3.9	9	4.7	0.86
SWR Frequency (Hz)	3.8	1.7	9	10	0.35
SW Amplitude (uV)	47	37	9	21	0.012
SWR CA1 SG Power (Z-score)	0.99	0.68	9	-2088	1
SWR CA1–CA3 Delta Coh.	-0.0017	-0.0086	9	-43139	1
SWR CA1–DG Delta Coh.	0.0046	-0.00038	9	-30365	1
CA3 SWR Frequency (Hz)	-2	-1.4	9	14	0.14
SWR Size (SD)	-0.53	-0.6	9	11	0.24

SWR CA3 SG Power (Z-score)	0.57	0.3	9	-936	1
SWR DG SG Power (Z-score)	0.43	0.17	9	-7482	1
PV-Cre/SST-Cre: Run Features	F β (n = 4)	M β (n = 3)	df	χ2	p
CA1 MUA (Hz)	11.02	0.13	9	16.26	0.06
CA3 MUA (Hz)	**335.91**	**2.59**	**9**	**23.31**	**0.0055**
DG MUA (Hz)	**336.24**	**2.71**	**9**	**23.12**	**0.0059**
CA1 SG Power (μV^2)	180	24	9	15	0.079
CA1–CA3 SG Coh.	0.032	0.0097	9	17	0.056
CA1–DG SG Coh.	0.031	0.11	9	22	0.011
CA1 SG Freq. (Hz)	-2	-1.4	9	17	0.051
CA1 Theta–SG Comod.	-0.00037	-0.00025	9	9.7	0.38
CA1 FG Power (μV^2)	28	30	9	18	0.033
CA1 SG/FG ratio	2.6	1.4	9	14	0.11
CA1–CA3 FG Coh.	0.0051	0.0009	9	13	0.18
CA1–DG FG Coh.	0.0012	0.0085	9	14	0.11
CA1 FG Freq (Hz)	3.1	1.3	9	17	0.046
CA1 Theta–FG Comod.	-0.001	-0.00061	9	9	0.44
CA3 SG Power (μV^2)	-5.8	12	9	17	0.043
DG SG Power (μV^2)	-66	1.3	9	15	0.088
CA3 SG Freq. (Hz)	-2.1	-1.3	9	17	0.043
DG SG Freq. (Hz)	-1.7	-1.1	9	17	0.052
CA3 Theta–SG Comod.	-0.00042	-0.00019	9	6	0.74
DG Theta–SG Comod.	-0.00054	-0.00031	9	14	0.11
CA3 FG Power (μV^2)	-2.5	-1.9	9	13	0.15
DG FG Power (μV^2)	-20	-12	9	14	0.11
CA3 SG/FG ratio	0.33	0.88	9	17	0.053
DG SG/FG ratio	0.28	0.45	9	16	0.07
CA3 FG Freq. (Hz)	3	0.93	9	17	0.049
DG FG Freq. (Hz)	3.3	1.4	9	15	0.089
CA3 Theta–FG Comod.	-0.00054	-0.00096	9	11	0.25
DG Theta–FG Comod.	-0.0011	-0.0023	9	13	0.17
CA1 Theta Power (μV^2)	1021	191	9	24	0.0051
CA3 Theta Power (μV^2)	-20	-332	9	17	0.052
DG Theta Power (μV^2)	-332	-951	9	21	0.012
CA1–CA3 Theta Coh.	0.06	-0.011	9	17	0.041
CA1–DG Theta Coh.	0.0093	-0.13	9	19	0.026
CA1 Theta Freq. (Hz)	0.36	0.23	9	13	0.17
CA3 Theta Freq. (Hz)	0.38	0.23	9	13	0.15
DG Theta Freq. (Hz)	0.39	0.33	9	13	0.14

835   Likelihood ratio test for sex-treatment interaction effects. Significant comparisons are bolded.

836

KEY RESOURCES TABLE

REAGENT or RESOURCE	SOURCE	IDENTIFIER
Antibodies		
Rat anti-SST	Millipore	Cat#MAB354; RRID:AB_2255365
Mouse anti-PV	Millipore	Cat#MAB1572; RRID:AB_2174013
Biotinylated rabbit anti-RFP	Abcam	Cat#ab34771; RRID:AB_777699
Donkey anti-rat AlexaFluor488	Thermo Fisher Scientific	Cat#A-21208; RRID:AB_2535794
Goat anti-rat AlexaFluor647	Thermo Fisher Scientific	Cat#A-21247; RRID:AB_141778
Donkey anti-mouse AlexaFluor647	Thermo Fisher Scientific	Cat#A-31571; RRID:AB_162542
Streptavidin AlexaFluor594	Sigma Aldrich	Cat#S6402
Bacterial and Virus Strains		
AAV5-hSyn-DIO-hM4D(Gi)-mCherry	UNC Viral Vector Core (Krashes et al., 2011)	N/A
AAV5-hSyn-DIO-mCherry	Addgene	RRID:Addgene_50459
Chemicals, Peptides, and Recombinant Proteins		
Ketamine	Henry Schein	Cat#1049007
Xylazine (Anased)	Henry Schein	Cat#1311139
Isofluorane	Henry Schein	Cat#029405
Buprenorphine	Henry Schein	Cat#055175
Ketofen	Henry Schein	Cat#005487
Avertin (2,2,2-Tribromoethanol)	Millipore Sigma	Cat# T48402
Dental Adhesive (Metabond)	Parkell	Cat#S396, S398 and S371
Dental Acrylic	Stoelting Co.	Cat#51459
Cresyl Violet Acetate	Sigma Aldrich	Cat#C5042
ProLong Gold with DAPI	Thermo Fisher Scientific	Cat#P36931
Deposited Data		
0–300 Hz filtered LFP, MUA spike times, mouse position tracking, and metadata for each electrode site, mouse, and recording session	This paper	Will be uploaded after paper acceptance
Experimental Models: Organisms/Strains		
Mouse: PVCre: $Pvalb^{tm1(cre)Arbr}$/J	Jackson Laboratory	MGI:3590684; RRID:IMSR_JAX:013044
Mouse: SSTCre: $Sst^{tm2.1(cre)Zjh}$/J	Jackson Laboratory	MGI:4838416; RRID:IMSR_JAX:008069
Software and Algorithms		
Custom scripts for this paper	This paper	Will be uploaded after paper acceptance

Trodes	SpikeGadgets	https://bitbucket.org/mkarlsso/trodes/downloads
NeuroQuery	Bitbucket	https://bitbucket.org/mkarlsso/neuroquery/src/master
MATLAB	Mathworks	N/A
Chronux	Cold Spring Harbor Laboratory	http://chronux.org
plot spread points	MATLAB Central File Exchange	https://www.mathworks.com/matlabcentral/fileexchange/37105-plot-spread-points-beeswarm-plot
Axon pCLAMP	Molecular Devices	https://mdc.custhelp.com/app/answers/detail/a_id/18779/~/axon%E2%84%A2pclamp%E2%84%A2-10-electrophysiology-data-acquisition-%26-analysis-software-download
IGOR Pro	WaveMetrics	https://www.wavemetrics.com/
Other		
Probe	Neuronexus	A4x8-400-200-704-CM32

837 **STAR METHODS**

838 **Lead Contact and Materials Availability**

839 This study did not generate any unique reagents. Further information and requests for resources

840 and reagents should be directed to and will be fulfilled by the Lead Contacts, Yadong Huang

841 (yadong.huang@gladstone.ucsf.edu) or Loren Frank (loren@phy.uscf.edu).

842

843 **EXPERIMENTAL MODEL AND SUBJECT DETAILS**

844 C57BL6/J mice with the SST-IRES-Cre allele (*Sst^{tm2.1(cre)Zjh}*/J) or the PV-IRES-Cre allele

845 (*Pvalb^{tm1(cre)Arbr}*/J) knocked-in (Hippenmeyer et al., 2005; Taniguchi et al., 2011) were originally

846 obtained from Jackson Laboratory. Equal numbers of PV-Cre, SST-Cre and PV-Cre/SST-Cre mice

847 were selected from littermates of a PV-Cre x SST-Cre cross. All animals were bred in-house using

848 trio breeding producing 10 pups per litter on average, which were weaned at 28 days. Equal

849 proportions of males and females aged 3–8 months were selected for each genotype and viral

850 vector. Within each genotype group and sex, mice were randomly assigned to receive either

851 hM4Di-mCherry vector or mCherry empty vector injection. Experimenters were blinded to

852 genotype during surgery and blinded to genotype and viral vector expression during all post-

853 operative behavior, recordings, and histology. Animals were housed in a pathogen-free barrier

854 facility on a 12h light cycle (lights on at 7am and off at 7pm) at 19–23°C and 30–70% humidity.

855 Animals were identified by ear punch under brief isofluorane anesthesia and genotyped by PCR

856 of a tail clipping at both weaning and perfusion. All animals otherwise received no procedures

857 except those reported in this study. Throughout the study, mice were singly housed. All animal

858 experiments were conducted in accordance with the guidelines and regulations of the National

859 Institutes of Health, the University of California, and the Gladstone Institutes under IACUC

860   protocol AN117112.

861

862   **METHOD DETAILS**

863   This study consisted of two cohorts. The first cohort (n = 9 PV-Cre, n = 10 SST-Cre, n = 6 PV-

864   Cre/SST-Cre) had home cage recordings (Figure 2) while the second cohort (n = 8 PV-Cre, n = 7

865   SST-Cre, n = 7 PV-Cre/SST-Cre, and n = 8 empty vector mice) had linear track recordings (Figure

866   4), then home cage recordings (Figure 2). In the second cohort, 1 PV-Cre and 1 SST-Cre animal

867   died between linear track and home cage recordings and so were not included in the analysis in

868   Figure 2 and Table S1.

869

870   **Surgery**

871   Mice were anesthetized by intraperitoneal injection of ketamine (60 mg/kg) and xylazine (30

872   mg/kg); anesthesia was maintained with 0.6–1.5% isoflurane given through a vaporizer and nose

873   cone. The head was secured with earbars and a tooth bar in a stereotaxic alignment system (Kopf

874   Instruments). Fur was removed from the scalp, which was then sterilized with alternating swabs

875   of chlorhexidine and 70% ethanol. The scalp was opened, sterilized with 3% hydrogen peroxide,

876   and thoroughly cleaned to reduce risk of tissue regrowth. 0.5 mm craniotomies were made at 1.95

877   mm AP and ± 1.5 mm ML from bregma for viral injection. 1 µL of 4.6 x 10^{12}vg/mL AAV5-hSyn-

878   DIO-hM4D(Gi)-mCherry (UNC Viral Vector Core; (Krashes et al., 2011)) or 7 x 10^{12}vg/mL

879   AAV5-hSyn-DIO-mCherry (Addgene) was injected at 2.1 mm below the surface of the brain

880   (Andrews-Zwilling et al., 2012; Stefanelli et al., 2016) at an infusion rate of 100nL/min. Skull

881   screws (FST) were inserted into craniotomies over the right frontal cortex and left parietal cortex

882   to anchor and support the implant, and were secured with dental adhesive (C&B Metabond,

883   Parkell). An additional 0.5 mm craniotomy was made over the right cerebellum for insertion of

884   the indifferent ground and reference wires. The craniotomy centered at -1.95 mm AP and 1.5 mm

885   ML from bregma and extended bidirectionally along the ML axis to 2 mm width to receive the

886   recording probe. The probes had four 5 mm shanks spaced 400 µm apart with 8 electrode sites per

887   shank and 200 µm spacing between sites (Neuronexus; configuration A4x8-400-200-704-CM32).

888   The probe was quickly lowered until the tip reached 2.2 mm below the surface of the brain, and

889   the reference and ground wire was inserted into the subdural space above the cerebellum. The

890   probe was cemented in place with dental acrylic and the scalp was closed with nylon sutures. Mice

891   were treated with 0.0375 mg/kg buprenorphine intraperitoneally and 5 mg/kg ketofen

892   subcutaneously 30–45 min after surgery, monitored until ambulatory, then monitored daily for 3

893   days. A minimum of 3 weeks was allowed for recovery and viral expression before recording.

894

895   **Electrophysiology**

896   Each animal was randomly assigned a time during the light cycle, and behavior and recordings

897   were always conducted with that animal at that same time each day ± 1 hour. CNO (NIMH, C-

898   929) in 1% DMSO in 0.9% sterile saline (CNO) or equivalent volume of 1% DMSO in 0.9% sterile

899   saline (vehicle) was administered via intraperitoneal injection at a dose of 2 mg/kg 1 hour prior to

900   data collection. Body weight was measured weekly during treatment and injection volume was

901   adjusted accordingly. Injections were well tolerated and had no adverse effects on health. Data

902   were collected on a Main Control Unit (SpikeGadgets) with simultaneous video tracking at 30

903   frames/s using Trodes software (SpikeGadgets).

904   During home cage recordings, data were collected, amplified, multiplexed, processed, and

905   digitized using a 32-channel upright headstage and commutator (SpikeGadgets) at 30 kHz. Data

906   were collected during 60 min home cage sessions for 6 days, alternating vehicle and CNO

907   administration. Home cages were changed to Alpha-dri bedding (Shepherd Specialty Papers) to

908   enable video tracking.

909   For linear track recordings, animals were screened for sufficient food motivation prior to

910   surgery. Each animal was restricted to 85–90% of its baseline weight then run on a 36 cm linear

911   track for 30 min sessions daily for 10 µL soy milk reward dispensed from custom automatic

912   solenoids controlled by an Environmental Control Unit (SpikeGadgets) with custom scripts.

913   Animals which did not achieve at least 180 pokes over 3 sessions were excluded from surgery.

914   Following surgery, animals ran for 30 min on linear track for 6 days, alternating vehicle and CNO

915   administration. Data were collected, amplified, multiplexed, processed, and digitized using a

916   wireless 32-channel mini logger headstage (SpikeGadgets) at 20 kHz.

917

918   **Histology**

919   Mice were deeply anesthetized with avertin, and a 30 µA current was passed through each

920   recording site for 2 s to generate small electrolytic lesions (Ugo Basile). Mice were then perfused

921   with 0.9% NaCl. The brains were removed and stored at 4°C, then fixed in 4% PFA for 2 days,

922   rinsed in PBS for 1 day, and cryoprotected in 30% sucrose for at least 2 days. Brains were cut into

923   30 µm coronal sections with a microtome (Leica) and stored in cryoprotectant at -20°C. Every

924   third section was stained with cresyl violet, then electrolytic lesion locations were observed under

925   a light microscope (Leica). Every tenth section was used for immunohistochemistry. Sections were

926   blocked and permeabilized in 10% normal donkey serum and 0.5% Triton X for 1 hour at room

927   temperature, and then incubated overnight at 4°C in 1:100 rat anti-SST (Millipore), 1:1000 mouse

928   anti-PV (Millipore), and 1:500 biotinylated rabbit anti-RFP (Abcam). Sections were then

929   incubated for 1 hour at room temperature in 1:1500 donkey anti-rat AlexaFluor488 (Thermo Fisher

930   Scientific) or 1:1500 goat anti-rat AlexaFluor647 (Thermo Fisher Scientific), 1:1500 donkey anti-

931   mouse AlexaFluor647 (Thermo Fisher Scientific), and 1:1000 Streptavidin AlexaFluor594 (Sigma

932   Aldrich) and mounted to slides using DAPI. Images were collected on a fluorescent microscope

933   (Keyence) and counted manually in ImageJ. 1 SST-Cre animal from the first cohort was excluded

934   from all analyses due to low viral expression. Representative images were adjusted for contrast

935   only.

936

937   ***Ex vivo* electrophysiology**

938   3–6 month old mice were stereotaxically injected with hM4D as described above, then the scalp

939   was sutured closed. 3 weeks following surgery to allow for viral expression, mice were deeply

940   anesthetized with isofluorane. The brain was rapidly removed and placed in 4°C slicing solution

941   comprised of 110 mM Choline Chloride, 2.5 mM KCl, 1.25 mM NaH_2PO_4, 26 mM $NaHCO_3$, 2

942   mM $CaCl_2$, 1.3 mM Na Pyruvate, 1 mM L-Ascorbic Acid, and 10 mM dextrose. 300μm sagittal

943   sections were cut using a vibratome (VT 1200s, Leica), transferred to a vapor interface chamber

944   aerated with 95% O_2 / 5% CO_2 gas mixture, and allowed to recover at 34°C for one hour prior to

945   recording. Sections were then transferred to a submerged recording chamber at 34°C perfused at

946   10 mL/min with oxygenated aCSF solution comprised of 124 mM NaCl, 26 mM $NaHCO_3$, 10 mM

947   Glucose, 1.25 mM NaH_2PO_4, 2.5 mM KCl, 1.25 mM $MgCl_2$, and 1.5 mM $CaCl_2$. SST^+ and PV^+

948   cells were visually identified in the DG by mCherry expression and morphology using a modified

949   Olympus BXW-51 microscope (Scientifica, Inc). Interneurons were recorded using patch-clamp

950   electrodes filled with an intracellular solution comprised of 125 mM K-gluconate, 10 mM KCl, 10

951   mM HEPES, 2 mM $MgCl_2$, 10 mM EGTA, 4 mM MgATP, 10 mM Na-phosphocreatine, and 3

952 mM Na₂GTP. CNO was dissolved to 1μM in aCSF and delivered through the perfusion system.

953 Whole cell recordings were performed using a Multiclamp 700B amplifier (Molecular Devices).

954 The signals were sampled at 10 kHz and digitized using Digidata 1550B with Axon pCLAMP

955 (Molecular Devices). Data was analyzed using custom scripts in IGOR Pro (WaveMetrics).

956

957 **Analysis of neural data**

958 Neural data was analyzed with custom software written in MATLAB (Mathworks) with

959 the Chronux toolbox (http://www.chronux.org) and Trodes to MATLAB software (SpikeGadgets).

960 The anatomical location of each electrode site was determined by examining Nissl-stained

961 histological sections, raw LFP traces, the SWR-triggered spectrogram signature, and dentate

962 spikes. Only DG sites with visually confirmed dentate spikes were included in analysis. Data were

963 data were referenced to a corpus callosum electrode, band-pass Butterworth filtered at 0.1–300

964 Hz, and then downsampled to 1 kHz and analyzed as LFP. All measurements were analyzed per

965 session and electrode site, then averaged across all sessions and all electrode sites within each

966 subregion. Thus, each mouse contributed a single number to all comparisons.

967 Raw LFP data during rest sessions were band-pass equiripple filtered at 125–200 Hz for

968 SWRs, 0–30 Hz for SWs, and 30–50 Hz for SG. SWRs were detected on the CA1 site closest to

969 the center of the pyramidal layer and defined by the Hilbert envelope of the ripple-filtered trace,

970 smoothed with a 4 ms Gaussian, exceeding 3 SD above baseline for at least 15 ms (Cheng and

971 Frank, 2008). Analysis was restricted to periods of extended immobility, after the mouse Gaussian

972 smoothed velocity had been < 1 cm/s for 30 seconds or more. SWRs were considered part of chains

973 if a second SWR event occurred within 200 ms of the end of an event. Instantaneous frequency

974 was defined by interpeak times during SWRs. SW amplitude was defined as the maximum absolute

975   value of the Hilbert envelope of the SW-filtered trace during SWRs. SWRs in CA3 were detected

976   on the site with the highest MUA and examined only when they coincided with an SWR detected

977   in CA1.

978   SWR-triggered spectrograms for each electrode site and SWR-triggered coherence

979   between regions were calculated with the multitaper method, as previously described (Carr et al.,

980   2012), with a 100 ms sliding window. Delta coherence was calculated as the difference between

981   the 100 ms window starting 400 ms before SWR onset and the 100 ms window after SWR onset;

982   SWRs that were preceded by SWRs within this window were excluded. For illustration in figures,

983   a 10 ms sliding window was used. SWR-associated SG power was calculated as the averaged z-

984   scored power over the 30–50 Hz frequency band 0–100 ms after ripple detection. SG power was

985   analyzed for three regions: CA1-sr, CA3 including pyr and sr, and DG including hilus and granule

986   cell layers. For CNO epochs, the mean and SD of the SG filtered signal from the vehicle epoch

987   recorded the day before were used for z-scoring.

988   For MUA analysis, data were referenced to a corpus callosum electrode, band-pass filtered

989   at 600–6000 Hz (Butterworth), and then events greater than 75 μV were treated as spikes. Sites

990   used for SWR detection were further verified to be in the CA1 pyramidal layer as they showed

991   large increases in MUA during SWRs. The site closest to the center of the cell layer, as determined

992   by highest MUA, was used for MUA analysis. For fast ripple analysis, data were downsampled to

993   5 kHz and band-pass equiripple filtered at 125–600 Hz, then events were detected in CA1 when

994   the Hilbert envelope of the ripple-filtered trace, smoothed with a 4 ms Gaussian, exceeded 3 SD

995   above baseline for at least 3 oscillations of the filtered trace. Events were classified as fast ripples

996   if the mean frequency was above 250 Hz.

997   Slow and fast gamma bands were defined by the frequencies with highest cross-frequency

998   coupling, as previously described (Colgin et al., 2009; Kemere et al., 2013). Raw LFP during linear

999   track sessions were then band-pass least squares FIR filtered at 5–11 Hz for theta, 20–50 Hz for

1000   SG, and 50–110 Hz for FG; these definitions matched those previously defined in mice using time-

1001   frequency methods (Cabral et al., 2014; Chen et al., 2011). Analysis was restricted to periods when

1002   the mouse Gaussian smoothed velocity exceeded 1 cm/s. Spectrograms were calculated with a

1003   multitaper method with a 1 s sliding window. Coherence was calculated using a multitaper method

1004   over all run periods. Instantaneous frequency was defined by interpeak times of the band filtered

1005   trace during all run periods. LFP during run epochs was analyzed for 5 regions: CA1 pyr, sr, and

1006   slm; CA3 including pyr and sr; and DG including hilus and granule cell layers.

1007

1008   **QUANTIFICATION AND STATISTICAL ANALYSIS**

1009   Statistics were computed using custom software written in MATLAB (Mathworks). Figures 6 and

1010   S5–S6 were plotted with plotSpread function (MATLAB Central File Exchange). Statistical test

1011   used, exact n, and exact p value are in figure legends; test statistic values and degrees of freedom

1012   are in corresponding supplementary tables. In all cases, n represents number of animals. No data

1013   were excluded based on statistical tests. 3 mice were excluded from analysis due to poor viral

1014   expression. Sample sizes were based on previous studies (Gan et al., 2017; Lovett-Barron et al.,

1015   2014; Stefanelli et al., 2016; Xia et al., 2017). Central values plotted in Figures 2–5 and S2–S4 are

1016   means and individual points are mean per animal, as indicated in figure legends. Central values

1017   plotted in Figures 6 and S5 are linear mixed effects model (LMM) fixed effect coefficients β ±

1018   95% confidence intervals and individual points are the fitted conditional response for each mouse,

1019   as indicated in figure legends.

1020   Data for LMMs were drawn from events in the case of SWRs, time bins in the case of

1021   continuous measures (1 min for SWR rate, 100 ms for MUA, 1 s for all others), or peaks in the

1022   case of continuous frequency. Normality and independence of errors was confirmed visually; when

1023   errors were not Gaussian, they were always right skewed, and so a log transform was applied. We

1024   constructed an LMM using the ML method and the formula *feature ~ group + (group|animal)*

1025   where group was vehicle or CNO for treatment comparison, PV-Cre or SST-Cre for vehicle

1026   baselines comparison, and male or female for sex comparison. We then used an F test to assess the

1027   evidence that the treatment fixed effect model was a better fit than the intercept-only model. To

1028   evaluate differences between treatment effects, we pooled data across two groups and used a

1029   likelihood ratio test to compare the model *feature ~ treatment + (treatment|animal)* to the model

1030   *feature ~ treatment:gentoype + (treatment:genotype|animal)* (or *feature ~ treatment:sex +*

1031   *(treatment:sex|animal)* in the case of Table S6) and used a χ^2 test to assess if the data were equally

1032   likely under both models. For table S1, we used paired t tests when data were normally distributed

1033   as shown by Shapiro-Wilk test and variances between groups were similar as shown by F test; we

1034   used Wilcoxon matched pairs signed rank tests otherwise. For correlations in Figures S2 and S3,

1035   data were normally distributed as shown by Shapiro-Wilk test, so we used Pearson correlations.

1036   Significance threshold was set by the Holm-Bonferroni correction across an experiment

1037   with $\alpha = 0.05$. Other family-wise error rate correction methods were tested with similar results. An

1038   experiment was defined as all comparisons made during either rest sessions (15 comparisons in

1039   Figures 2, 3, and S2) or run sessions (36 comparisons in Figures 4, 5, S3, and S4) in a single

1040   genotype or between genotypes. Only p-values that met this threshold are displayed as significant

1041   in figures and tables.

1042

1043   **DATA AND SOFTWARE AVAILABILITY**

1044   The data generated during this study will be deposited on CRCNS.org upon acceptance for

1045   publication. The custom software generated during this study is deposited at

1046   https://github.com/emilyasterjones/interneurons_modulate_drive.

1047

1048   **REFERENCES**

1049   Abbas, A.I., Sundiang, M.J.M., Henoch, B., Morton, M.P., Bolkan, S.S., Park, A.J., Harris, A.Z.,

1050   Kellendonk, C., and Gordon, J.A. (2018). Somatostatin Interneurons Facilitate Hippocampal-

1051   Prefrontal Synchrony and Prefrontal Spatial Encoding. Neuron *100*, 926-939.e3.

1052   Andrews-Zwilling, Y., Bien-Ly, N., Xu, Q., Li, G., Bernardo, A., Yoon, S.Y., Zwilling, D., Yan,

1053   T.X., Chen, L., and Huang, Y. (2010). Apolipoprotein E4 causes age- and Tau-dependent

1054   impairment of GABAergic interneurons, leading to learning and memory deficits in mice. J

1055   Neurosci *30*, 13707–13717.

1056   Andrews-Zwilling, Y., Gillespie, A.K., Kravitz, A. V., Nelson, A.B., Devidze, N., Lo, I., Yoon,

1057   S.Y., Bien-Ly, N., Ring, K., Zwilling, D., et al. (2012). Hilar GABAergic interneuron activity

1058   controls spatial learning and memory retrieval. PLoS One *7*, e40555.

1059   Antonoudiou, P., Tan, Y.L., Kontou, G., Upton, A.L., and Mann, E.O. (2020). Parvalbumin and

1060   Somatostatin Interneurons Contribute to the Generation of Hippocampal Gamma Oscillations. J.

1061   Neurosci.

1062   Axmacher, N., Henseler, M.M., Jensen, O., Weinreich, I., Elger, C.E., and Fell, J. (2010). Cross-

1063   frequency coupling supports multi-item working memory in the human hippocampus. Proc. Natl.

1064   Acad. Sci. *107*, 3228–3233.

1065   Behrens, C.J., van den Boom, L.P., and Heinemann, U. (2007). Effects of the GABA $_A$ receptor

1066   antagonists bicuculline and gabazine on stimulus-induced sharp wave-ripple complexes in adult

1067   rat hippocampus *in vitro*. Eur. J. Neurosci. *25*, 2170–2181.

1068   Blasco-Ibáñez, J.M., and Freund, T.F. (1995). Synaptic Input of Horizontal Interneurons in

1069   Stratum Oriens of the Hippocampal CA1 Subfield: Structural Basis of Feed-back Activation.

1070   Eur. J. Neurosci. *7*, 2170–2180.

1071   Bragin, A., Jandó, G., Nádasdy, Z., van Landeghem, M., and Buzsáki, G. (1995a). Dentate EEG

1072   spikes and associated interneuronal population bursts in the hippocampal hilar region of the rat.

1073   J. Neurophysiol. *73*, 1691–1705.

1074   Bragin, A., Jandó, G., Nádasdy, Z., Hetke, J., Wise, K., Buzsáki, G., Szabó, G., Freund, T.F., and

1075   Hájos, N. (1995b). Gamma (40-100 Hz) oscillation in the hippocampus of the behaving rat. J.

1076   Neurosci. *15*, 47–60.

1077   Buzsáki, G. (1989). Two-stage model of memory trace formation: A role for "noisy" brain states.

1078   Neuroscience *31*, 551–570.

1079   Buzsáki, G., Leung, L., and Vanderwolf, C.H. (1983). Cellular bases of hippocampal EEG in the

1080   behaving rat. Brain Res. *287*, 139–171.

1081   Buzsáki, G., Horváth, Z., Urioste, R., Hetke, J., and Wise, K. (1992). High-frequency network

1082   oscillation in the hippocampus. Science (80-.). *256*, 1025–1027.

1083   Cabral, H.O., Vinck, M., Fouquet, C., Pennartz, C.M.A., Rondi-Reig, L., and Battaglia, F.P.

1084   (2014). Oscillatory dynamics and place field maps reflect hippocampal ensemble processing of

1085   sequence and place memory under NMDA receptor control. Neuron *81*, 402–415.

1086   Caputi, A., Fuchs, E.C., Allen, K., Le Magueresse, C., and Monyer, H. (2012). Selective

1087   Reduction of AMPA Currents onto Hippocampal Interneurons Impairs Network Oscillatory

1088   Activity. PLoS One *7*, e37318.

1089   Carr, M.F., and Frank, L.M. (2012). A single microcircuit with multiple functions: state

1090 dependent information processing in the hippocampus. Curr. Opin. Neurobiol. *22*, 704–708.

1091 Carr, M.F., Karlsson, M.P., and Frank, L.M. (2012). Transient Slow Gamma Synchrony

1092 Underlies Hippocampal Memory Replay. Neuron *75*, 700–713.

1093 Cayzac, S., Mons, N., Ginguay, A., Allinquant, B., Jeantet, Y., and Cho, Y.H. (2015). Altered

1094 hippocampal information coding and network synchrony in APP-PS1 mice. Neurobiol. Aging

1095 *36*, 3200–3213.

1096 Chen, G., Zhang, Y., Li, X., Zhao, X., Ye, Q., Lin, Y., Tao, H.W., Rasch, M.J., and Zhang, X.

1097 (2017). Distinct Inhibitory Circuits Orchestrate Cortical beta and gamma Band Oscillations.

1098 Neuron *96*, 1403-1418.e6.

1099 Chen, Z., Resnik, E., McFarland, J.M., Sakmann, B., and Mehta, M.R. (2011). Speed Controls

1100 the Amplitude and Timing of the Hippocampal Gamma Rhythm. PLoS One *6*, e21408.

1101 Cheng, S., and Frank, L.M. (2008). New experiences enhance coordinated neural activity in the

1102 hippocampus. Neuron *57*, 303–313.

1103 Ciupek, S.M., Cheng, J., Ali, Y.O., Lu, H.-C., and Ji, D. (2015). Progressive Functional

1104 Impairments of Hippocampal Neurons in a Tauopathy Mouse Model. J. Neurosci. *35*, 8118–

1105 8131.

1106 Colgin, L.L. (2015). Theta-gamma coupling in the entorhinal-hippocampal system. Curr. Opin.

1107 Neurobiol. *31*, 45–50.

1108 Colgin, L.L. (2016). Rhythms of the hippocampal network. Nat. Rev. Neurosci. *17*, 239–249.

1109 Colgin, L.L., Denninger, T., Fyhn, M., Hafting, T., Bonnevie, T., Jensen, O., Moser, M.-B., and

1110 Moser, E.I. (2009). Frequency of gamma oscillations routes flow of information in the

1111 hippocampus. Nature *462*, 353–357.

1112 Cowen, S.L., Gray, D.T., Wiegand, J.-P.P.L., Schimanski, L.A., and Barnes, C.A. (2018). Age-

1113   associated changes in waking hippocampal sharp-wave ripples. Hippocampus *30*, 28–38.

1114   Csicsvari, J., Hirase, H., Mamiya, A., and Buzsáki, G. (2000). Ensemble patterns of hippocampal

1115   CA3-CA1 neurons during sharp wave-associated population events. Neuron *28*, 585–594.

1116   Drexel, M., Romanov, R.A., Wood, J., Weger, S., Heilbronn, R., Wulff, P., Tasan, R.O.,

1117   Harkany, T., and Sperk, G. (2017). Selective Silencing of Hippocampal Parvalbumin

1118   Interneurons Induces Development of Recurrent Spontaneous Limbic Seizures in Mice. J.

1119   Neurosci. *37*, 8166–8179.

1120   Ego-Stengel, V., and Wilson, M.A. (2010). Disruption of ripple-associated hippocampal activity

1121   during rest impairs spatial learning in the rat. Hippocampus *20*, 1–10.

1122   Ewell, L.A., Fischer, K.B., Leibold, C., Leutgeb, S., and Leutgeb, J.K. (2019). The impact of

1123   pathological high-frequency oscillations on hippocampal network activity in rats with chronic

1124   epilepsy. Elife *8*, e42148.

1125   Fernández-Ruiz, A., Oliva, A., Nagy, G.A., Maurer, A.P., Berényi, A., and Buzsáki, G. (2017).

1126   Entorhinal-CA3 Dual-Input Control of Spike Timing in the Hippocampus by Theta-Gamma

1127   Coupling. Neuron *93*, 1213-1226.e5.

1128   Fernández-Ruiz, A., Oliva, A., Fermino de Oliveira, E., Rocha-Almeida, F., Tingley, D., and

1129   Buzsáki, G. (2019). Long-duration hippocampal sharp wave ripples improve memory. Science

1130   *364*, 1082–1086.

1131   Foffani, G., Uzcategui, Y.G., Gal, B., Menendez de la Prida, L., Szabo, I., Sik, A., Buzsáki, G.,

1132   Wilent, W.B., and Higley, M.J. (2007). Reduced Spike-Timing Reliability Correlates with the

1133   Emergence of Fast Ripples in the Rat Epileptic Hippocampus. Neuron *55*, 930–941.

1134   Freund, T.F., and Buzsáki, G. (1998). Interneurons of the hippocampus. Hippocampus *6*, 347–

1135   470.

1136   Funk, C.M., Peelman, K., Bellesi, M., Marshall, W., Cirelli, C., and Tononi, G. (2017). Role of

1137   Somatostatin-Positive Cortical Interneurons in the Generation of Sleep Slow Waves. J. Neurosci.

1138   *37*, 9132–9148.

1139   Gan, J., Weng, S., Pernía-Andrade, A.J., Csicsvari, J., and Jonas, P. (2017). Phase-Locked

1140   Inhibition, but Not Excitation, Underlies Hippocampal Ripple Oscillations in Awake Mice In

1141   Vivo. Neuron *93*, 308–314.

1142   Gillespie, A.K., Jones, E.A., Lin, Y.-H., Karlsson, M.P., Kay, K., Yoon, S.Y., Tong, L.M., Nova,

1143   P., Carr, J.S., Frank, L.M., et al. (2016). Apolipoprotein E4 causes age-dependent disruption of

1144   slow gamma oscillations during hippocampal sharp-wave ripples. Neuron *90*, 740–751.

1145   Girardeau, G., Benchenane, K., Wiener, S.I., Buzsáki, G., and Zugaro, M.B. (2009). Selective

1146   suppression of hippocampal ripples impairs spatial memory. Nat. Neurosci. *12*, 1222–1223.

1147   Gulyás, A.I., Megías, M., Emri, Z., Freund, T.F., Whittington, M., and Buzsáki, G. (1999). Total

1148   number and ratio of excitatory and inhibitory synapses converging onto single interneurons of

1149   different types in the CA1 area of the rat hippocampus. J. Neurosci. *19*, 10082–10097.

1150   Guo, N., Soden, M.E., Herber, C., Kim, M.T., Besnard, A., Lin, P., Ma, X., Cepko, C.L.,

1151   Zweifel, L.S., and Sahay, A. (2018). Dentate granule cell recruitment of feedforward inhibition

1152   governs engram maintenance and remote memory generalization. Nat. Med. *24*, 438–449.

1153   Hakim, R., Shamardani, K., and Adesnik, H. (2018). A neural circuit for gamma-band coherence

1154   across the retinotopic map in mouse visual cortex. Elife *7*, e28569.

1155   Harris, K.D., Hochgerner, H., Skene, N.G., Magno, L., Katona, L., Bengtsson Gonzales, C.,

1156   Somogyi, P., Kessaris, N., Linnarsson, S., and Hjerling-Leffler, J. (2018). Classes and continua

1157   of hippocampal CA1 inhibitory neurons revealed by single-cell transcriptomics. PLOS Biol. *16*,

1158   e2006387.

1159   Hippenmeyer, S., Vrieseling, E., Sigrist, M., Portmann, T., Laengle, C., Ladle, D.R., and Arber,

1160   S. (2005). A developmental switch in the response of DRG neurons to ETS transcription factor

1161   signaling. PLoS Biol. *3*, e159.

1162   Iaccarino, H.F., Singer, A.C., Martorell, A.J., Rudenko, A., Gao, F., Gillingham, T.Z., Mathys,

1163   H., Seo, J., Kritskiy, O., Abdurrob, F., et al. (2016). Gamma frequency entrainment attenuates

1164   amyloid load and modifies microglia. Nature *540*, 230–235.

1165   Jadhav, S.P., Kemere, C., German, P.W., and Frank, L.M. (2012). Awake Hippocampal Sharp-

1166   Wave Ripples Support Spatial Memory. Science (80-.). *336*, 1454–1458.

1167   Jinno, S., and Kosaka, T. (2000). Colocalization of parvalbumin and somatostatin-like

1168   immunoreactivity in the mouse hippocampus: Quantitative analysis with optical disector. J.

1169   Comp. Neurol. *428*, 377–388.

1170   Jinno, S., and Kosaka, T. (2002). Patterns of expression of calcium binding proteins and neuronal

1171   nitric oxide synthase in different populations of hippocampal GABAergic neurons in mice. J.

1172   Comp. Neurol. *449*, 1–25.

1173   Jinno, S., and Kosaka, T. (2003). Patterns of expression of neuropeptides in GABAergic

1174   nonprincipal neurons in the mouse hippocampus: Quantitative analysis with optical disector. J.

1175   Comp. Neurol. *461*, 333–349.

1176   Jones, E.A., Gillespie, A.K., Yoon, S.Y., Frank, L.M., and Huang, Y. (2019). Early Hippocampal

1177   Sharp-Wave Ripple Deficits Predict Later Learning and Memory Impairments in an Alzheimer's

1178   Disease Mouse Model. Cell Rep. *29*, 2123-2133.e4.

1179   Kay, K., and Frank, L.M. (2019). Three brain states in the hippocampus and cortex.

1180   Hippocampus *29*, 184–238.

1181   Kemere, C., Carr, M.F., Karlsson, M.P., and Frank, L.M. (2013). Rapid and continuous

1182 modulation of hippocampal network state during exploration of new places. PLoS One *8*,

1183 e73114.

1184 Kim, D., Jeong, H., Lee, J., Ghim, J.-W., Her, E.S., Lee, S.-H., and Jung, M.W. (2016). Distinct

1185 Roles of Parvalbumin- and Somatostatin-Expressing Interneurons in Working Memory. Neuron

1186 *92*, 902–915.

1187 Klausberger, T., and Somogyi, P. (2008). Neuronal diversity and temporal dynamics: the unity of

1188 hippocampal circuit operations. Science (80-.). *321*, 53–57.

1189 Krashes, M.J., Koda, S., Ye, C., Rogan, S.C., Adams, A.C., Cusher, D.S., Maratos-Flier, E.,

1190 Roth, B.L., and Lowell, B.B. (2011). Rapid, reversible activation of AgRP neurons drives

1191 feeding behavior in mice. J. Clin. Invest. *121*, 1424–1428.

1192 Kuki, T., Fujihara, K., Miwa, H., Tamamaki, N., Yanagawa, Y., and Mushiake, H. (2015).

1193 Contribution of parvalbumin and somatostatin-expressing GABAergic neurons to slow

1194 oscillations and the balance in beta-gamma oscillations across cortical layers. Front Neural

1195 Circuits *9*, 1–12.

1196 Kvitsiani, D., Ranade, S., Hangya, B., Taniguchi, H., Huang, J.Z., and Kepecs, A. (2013).

1197 Distinct behavioural and network correlates of two interneuron types in prefrontal cortex. Nature

1198 *498*, 363–366.

1199 Lee, C.-T., Kao, M.-H., Hou, W.-H., Wei, Y.-T., Chen, C.-L., and Lien, C.-C. (2016). Causal

1200 Evidence for the Role of Specific GABAergic Interneuron Types in Entorhinal Recruitment of

1201 Dentate Granule Cells. Sci. Rep. *6*, 36885.

1202 Leung, L., Andrews-Zwilling, Y., Yoon, S.Y., Jain, S., Ring, K., Dai, J., Wang, M.M., Tong, L.,

1203 Walker, D., and Huang, Y. (2012). Apolipoprotein E4 causes age- and sex-dependent

1204 impairments of hilar GABAergic interneurons and learning and memory deficits in mice. PLoS

1205   One *7*, e53569.

1206   López-Madrona, V.J., Pérez-Montoyo, E., Álvarez-Salvado, E., Moratal, D., Herreras, O.,

1207   Pereda, E., Mirasso, C.R., and Canals, S. (2020). Different theta frameworks coexist in the rat

1208   hippocampus and are coordinated during memory-guided and novelty tasks. Elife *9*.

1209   Lovett-Barron, M., Turi, G.F., Kaifosh, P., Lee, P.H., Bolze, F., Sun, X.-H., Nicoud, J.-F.,

1210   Zemelman, B. V., Sternson, S.M., and Losonczy, A. (2012). Regulation of neuronal input

1211   transformations by tunable dendritic inhibition. Nat. Neurosci. *15*, 423–430, S1-3.

1212   Lovett-Barron, M., Kaifosh, P., Kheirbek, M.A., Danielson, N., Zaremba, J.D., Reardon, T.R.,

1213   Turi, G.F., Hen, R., Zemelman, B. V., and Losonczy, A. (2014). Dendritic inhibition in the

1214   hippocampus supports fear learning. Science *343*, 857–863.

1215   Maurer, A.P., Cowen, S.L., Burke, S.N., Barnes, C.A., and McNaughton, B.L. (2006). Phase

1216   precession in hippocampal interneurons showing strong functional coupling to individual

1217   pyramidal cells. J. Neurosci. *26*, 13485–13492.

1218   McKenzie, S. (2017). Inhibition shapes the organization of hippocampal representations.

1219   Hippocampus *28*, 659–671.

1220   Miao, C., Cao, Q., Moser, M.-B., and Moser, E.I. (2017). Parvalbumin and Somatostatin

1221   Interneurons Control Different Space-Coding Networks in the Medial Entorhinal Cortex. Cell

1222   *171*, 507-521.e17.

1223   Middleton, S.J., and McHugh, T.J. (2016). Silencing CA3 disrupts temporal coding in the CA1

1224   ensemble. Nat. Neurosci. *19*, 945–951.

1225   Miles, R., Tóth, K., Gulyás, A.I., Hájos, N., and Freund, T.F. (1996). Differences between

1226   Somatic and Dendritic Inhibition in the Hippocampus. Neuron *16*, 815–823.

1227   Nakashiba, T., Buhl, D.L., McHugh, T.J., and Tonegawa, S. (2009). Hippocampal CA3 output is

1228   crucial for ripple-associated reactivation and consolidation of memory. Neuron *62*, 781–787.

1229   Nicole, O., Hadzibegovic, S., Gajda, J., Bontempi, B., Bem, T., and Meyrand, P. (2016). Soluble

1230   amyloid beta oligomers block the learning-induced increase in hippocampal sharp wave-ripple

1231   rate and impair spatial memory formation. Sci. Rep. *6*, 22728.

1232   Niethard, N., Ngo, H.-V. V, Ehrlich, I., and Born, J. (2018). Cortical circuit activity underlying

1233   sleep slow oscillations and spindles. Proc. Natl. Acad. Sci. *115*, E9220–E9229.

1234   Oliva, A., Fernández-Ruiz, A., Fermino de Oliveira, E., and Buzsáki, G. (2018). Origin of

1235   Gamma Frequency Power during Hippocampal Sharp-Wave Ripples. Cell Rep. *25*, 1693–1700.

1236   Ormond, J., McNaughton, B.L., and Moser, E.I. (2015). Place field expansion after focal MEC

1237   inactivations is consistent with loss of Fourier components and path integrator gain reduction.

1238   Proc. Natl. Acad. Sci. U. S. A. *112*, 4116–4121.

1239   Ramirez-Villegas, J.F., Logothetis, N.K., and Besserve, M. (2015). Diversity of sharp-wave–

1240   ripple LFP signatures reveals differentiated brain-wide dynamical events. Proc. Natl. Acad. Sci.

1241   *112*, E6379–E6387.

1242   Ramirez-Villegas, J.F., Willeke, K.F., Logothetis, N.K., and Besserve, M. (2018). Dissecting the

1243   Synapse- and Frequency-Dependent Network Mechanisms of In Vivo Hippocampal Sharp

1244   Wave-Ripples. Neuron *100*, 1224-1240.e13.

1245   Royer, S., Zemelman, B. V., Losonczy, A., Kim, J., Chance, F., Magee, J.C., and Buzsáki, G.

1246   (2012). Control of timing, rate and bursts of hippocampal place cells by dendritic and somatic

1247   inhibition. Nat. Neurosci. *15*, 769–775.

1248   Schlesiger, M.I., Cannova, C.C., Boublil, B.L., Hales, J.B., Mankin, E.A., Brandon, M.P.,

1249   Leutgeb, J.K., Leibold, C., and Leutgeb, S. (2015). The medial entorhinal cortex is necessary for

1250   temporal organization of hippocampal neuronal activity. Nat. Neurosci. *18*, 1123–1132.

1251   Sik, A., Penttonen, M., Ylinen, A., Buzsáki, G., Wise, K., and Buzsáki, G. (1995). Hippocampal

1252   CA1 interneurons: an in vivo intracellular labeling study. J. Neurosci. *15*, 6651–6665.

1253   Sik, A., Penttonen, M., and Buzsáki, G. (1997). Interneurons in the Hippocampal Dentate Gyrus:

1254   an In Vivo intracellular Study. Eur. J. Neurosci. *9*, 573–588.

1255   Sosa, M., Gillespie, A.K., and Frank, L.M. (2018). Neural Activity Patterns Underlying Spatial

1256   Coding in the Hippocampus. In Current Topics in Behavioral Neuroscience, Volume 37,

1257   (Springer Berlin Heidelberg), pp. 43–100.

1258   Spampanato, J., and Dudek, F.E. (2017). Targeted Interneuron Ablation in the Mouse

1259   Hippocampus Can Cause Spontaneous Recurrent Seizures. ENeuro *4*, ENEURO.0130-17.2017.

1260   Spiegel, A.M., Koh, M.T., Vogt, N.M., Rapp, P.R., and Gallagher, M. (2013). Hilar interneuron

1261   vulnerability distinguishes aged rats with memory impairment. J. Comp. Neurol. *521*, 3508–

1262   3523.

1263   Stark, E., Roux, L., Eichler, R., Senzai, Y., Royer, S.S., and Buzsáki, G. (2014). Pyramidal Cell-

1264   Interneuron Interactions Underlie Hippocampal Ripple Oscillations. Neuron *83*, 467–480.

1265   Stefanelli, T., Bertollini, C., Lüscher, C., Muller, D., and Mendez, P. (2016). Hippocampal

1266   Somatostatin Interneurons Control the Size of Neuronal Memory Ensembles. Neuron *89*, 1074–

1267   1085.

1268   Takács, V.T., Klausberger, T., Somogyi, P., Freund, T.F., and Gulyás, A.I. (2012). Extrinsic and

1269   local glutamatergic inputs of the rat hippocampal CA1 area differentially innervate pyramidal

1270   cells and interneurons. Hippocampus *22*, 1379–1391.

1271   Taniguchi, H., He, M., Wu, P., Kim, S., Paik, R., Sugino, K., Kvitsiani, D., Fu, Y., Lu, J., Lin,

1272   Y., et al. (2011). A resource of Cre driver lines for genetic targeting of GABAergic neurons in

1273   cerebral cortex. Neuron *71*, 995–1013.

1274 Udakis, M., Pedrosa, V., Chamberlain, S.E.L., Clopath, C., and Mellor, J.R. (2020). Interneuron-

1275 specific plasticity at parvalbumin and somatostatin inhibitory synapses onto CA1 pyramidal

1276 neurons shapes hippocampal output. Nat. Commun. *11*, 4395.

1277 Valero, M., Averkin, R.G., Fernandez-Lamo, I., Aguilar, J., Lopez-Pigozzi, D., Brotons-Mas,

1278 J.R., Cid, E., Tamas, G., and Menendez de la Prida, L. (2017). Mechanisms for Selective Single-

1279 Cell Reactivation during Offline Sharp-Wave Ripples and Their Distortion by Fast Ripples.

1280 Neuron *94*, 1234-1247.e7.

1281 Veit, J., Hakim, R., Jadi, M.P., Sejnowski, T.J., and Adesnik, H. (2017). Cortical gamma band

1282 synchronization through somatostatin interneurons. Nat Neurosci *20*, 951–959.

1283 Wheeler, D.W., White, C.M., Rees, C.L., Komendantov, A.O., Hamilton, D.J., and Ascoli, G.A.

1284 (2015). Hippocampome.org: a knowledge base of neuron types in the rodent hippocampus. Elife

1285 *4*, e09960.

1286 Wiegand, J.-P.L., Gray, D.T., Schimanski, L.A., Lipa, P., Barnes, C.A., and Cowen, S.L. (2016).

1287 Age Is Associated with Reduced Sharp-Wave Ripple Frequency and Altered Patterns of

1288 Neuronal Variability. J. Neurosci. *36*, 5650–5660.

1289 Wilson, N.R., Runyan, C.A., Wang, F.L., and Sur, M. (2012). Division and subtraction by

1290 distinct cortical inhibitory networks in vivo. Nature *488*, 343–348.

1291 Wu, F., Stark, E., and Ku, P. (2015). Monolithically Integrated m LEDs on Silicon Neural Probes

1292 for High-Resolution Optogenetic Studies in Behaving Animals. Neuron *88*, 1136–1148.

1293 Xia, F., Richards, B.A., Tran, M.M., Josselyn, S.A., Takehara-Nishiuchi, K., and Frankland,

1294 P.W. (2017). Parvalbumin-positive interneurons mediate neocortical-hippocampal interactions

1295 that are necessary for memory consolidation. Elife *6*, e27868.

1296 Yamamoto, J., and Tonegawa, S. (2017). Direct Medial Entorhinal Cortex Input to Hippocampal

1297   CA1 Is Crucial for Extended Quiet Awake Replay. Neuron *96*, 217-227.e4.

1298   Yamamoto, J., Suh, J., Takeuchi, D., and Tonegawa, S. (2014). Successful execution of working

1299   memory linked to synchronized high-frequency gamma oscillations. Cell *157*, 845–857.

1300   Ylinen, A., Bragin, A., Nádasdy, Z., Jandó, G., Szabó, I., Sik, A., and Buzsáki, G. (1995). Sharp

1301   wave-associated high-frequency oscillation (200 Hz) in the intact hippocampus: network and

1302   intracellular mechanisms. J. Neurosci. *15*, 30–46.

1303   Zou, D., Chen, L., Deng, D., Jiang, D., Dong, F., McSweeney, C., Zhou, Y., Liu, L., Chen, G.,

1304   Wu, Y., et al. (2016). DREADD in parvalbumin interneurons of the dentate gyrus modulates

1305   anxiety, social interaction and memory extinction. Curr. Mol. Med. *16*, 91–102.

1306